Optimal Design of Hybrid Composite Flywheel Rotor

Phase II

A Final Report

To

THE AIR FORCE OFFICE OF SCIENTIFIC RESEARCH

Prepared By

Prof. Sung Kyu Ha

Dong-Jin Kim

Young-Bok Yoon

Eun-Ju Ha

Dept. of Mech. Eng., Hanyang University

sungha@hanyang.ac.kr

April 2003

20041119 036

1

REPORT DOCUMENTATION PAGE

The public reporting burden for this collection of information is estimated to average 1 hour per response, including the time for reviewing instructions, searching existing data sources, gathering and maintaining the data needed, and completing and reviewing the collection of information. Send comments regarding this burden estimate or any other aspect of this collection of information, including suggestions for reducing the burden, to Department of Defense, Washington Headquarters Services, Directorate for Information Operations and Reports (0704-0188), 1215 Jefferson Davis Highway, Suite 1204, Arlington, VA 22202-4302. Respondents should be aware that notwithstanding any other provision of law, no person shall be subject to any penalty for failing to comply with a collection of information if it does not display a currently valid OMB control number.
PLEASE DO NOT RETURN YOUR FORM TO THE ABOVE ADDRESS.

1. REPORT DATE (DD-MM-YYYY)	2. REPORT TYPE	3. DATES COVERED (From - To)
22-01-2002	Final	24-Aug-2001 to 7-Apr-2003

4. TITLE AND SUBTITLE

Optimal Design of Hybrid Composite Flywheel Rotor – Phase II

5a. CONTRACT NUMBER
F6256201PM014

5b. GRANT NUMBER

5c. PROGRAM ELEMENT NUMBER

6. AUTHOR(S)

Prof. Sung Kyu Ha

5d. PROJECT NUMBER

5e. TASK NUMBER

5f. WORK UNIT NUMBER

7. PERFORMING ORGANIZATION NAME(S) AND ADDRESS(ES)
Hanyang University
Sa1-dong, Ansan-si
Kyungi-do 425-791
Korea (South)

8. PERFORMING ORGANIZATION REPORT NUMBER
N/A

9. SPONSORING/MONITORING AGENCY NAME(S) AND ADDRESS(ES)

AOARD
UNIT 45002
APO AP 96337-5002

10. SPONSOR/MONITOR'S ACRONYM(S)
AOARD

11. SPONSOR/MONITOR'S REPORT NUMBER(S)
AOARD-014026

12. DISTRIBUTION/AVAILABILITY STATEMENT

Approved for public release; distribution is unlimited.

13. SUPPLEMENTARY NOTES

14. ABSTRACT
This report summarizes three related efforts on optimization of composite flywheel rotors:

1. The effects of angles of filament winding on residual strains. These strains strongly affect mechanical performance.

2. The effects of rotor size and matrix epoxy system on residual strains and use of hybrid designs to optimize performance.

3. Development of a stress-analysis module and a software package to optimize flywheel-rotor design.

15. SUBJECT TERMS

Composite Materials, Flywheel Rotor

16. SECURITY CLASSIFICATION OF:			17. LIMITATION OF ABSTRACT	18. NUMBER OF PAGES	19a. NAME OF RESPONSIBLE PERSON
a. REPORT	b. ABSTRACT	c. THIS PAGE			Kenneth C. Goretta, Ph.D.
U	U	U	UU	54	19b. TELEPHONE NUMBER (Include area code) +81-3-5410-4409

SUMMARY

An optimization design tool has been developed for a flywheel rotor of fiber-reinforced composite materials. This tool specially considered the process-induced residual strains using an effective temperature. In the second period of the current project, most endeavors have been devoted to measure the residual strains of both helically wound rotors and hybrid multi-ring rotors. We have developed a new epoxy system which can decrease the residual strains by about 60 % compared to the conventional high temperature cure epoxy system. This report consists of three parts: Part I. The investigation of new epoxy systems; Part II. The effects of the helical winding angles on the residual strains; Part III. Development of flywheel rotor optimization tool, FlyOpt considering the residual strains.

The first part discusses the effects of filament winding angles on the residual strains and through-thickness material properties of a thick filament wound composite cylinders. The filament wound cylinders of 37.5 mm inner radius with a 75 mm radial thickness were manufactured using E-Glass fibers and Epoxy resin. The cylinders were sliced along the radial direction, and the through-thickness properties and the residual strains were measured. The through thickness properties were measured from 90 (hoop) to 60 degree wound cylinders, i.e., the radial Young's Moduli, the coefficients of thermal expansion, and the radial tensile strength. Significant decrease in the residual strains in the radial direction was noticed as the winding angles decrease; 1.23, 0.99, and 0.54 x 10^{-3} for 90, 75 and 60 degree winding angles. The residual strains were successfully predicted using the effective temperature drop of 140 °C in both two-dimensional analysis and three-dimensional FEM.

The second part discusses the effects of rotor sizes and different epoxy systems on the process-induced residual strains accumulated within wet-filament wound thick hybrid multi-ring composite rotors. Three different epoxy systems which cure at different temperature profiles were considered: high, middle, low (room) temperature cure epoxy systems. To evaluate the characteristics of the epoxy systems, the radial stiffness and strength and the coefficients of thermal expansion were measured from the Glass and

2

Graphite rotors. Hybrid two-ring composite rotors of Glass and Graphite fibers with equal thickness were manufactured for three different inner to outer radius ratios, i.e., 1.5, 2.0 and 2.5. A split ring method was then used to measure the radial and circumferential residual strains within the rotors, following liquid penetration tests to detect delaminations on the surfaces. Delaminations were observed in the high temperature cured rotors of radius ratios 2.0 and 2.5. The maximum radial stresses are observed to occur always at the interface between the Glass and Graphite rings. The measured residual strains are successfully predicted using a two dimensional stress analysis with an effective temperature drop. It is shown that the middle temperature cured rotor attains as high strength as the high temperature cured rotor while reducing significantly the residual strains.

The third or final part present how the stress analysis module was developed and linked to an optimization program in which the design variables, e.g., the thickness of each hybrid ring and winding angles can be optimized for the various size and material sequences of the composite flywheel rotor with a consideration of both the residual stresses and the rotational centrifugal stresses. The program FlyOpt has been further updated to incorporate the current experimental results and to have a user-interface convenient for designers of a flywheel composite rotor.

Currently, the developed program is successfully utilized by Structures and Composites Laboratory in Stanford University headed by Prof. Steve Tsai, and Korean Institutes of Machine and Machinery in Daedug, Korea. As a result of the current research, two papers were submitted for technical publication: the manuscript in the Part I to Composites Science and Technology, and the other manuscript in the Part II to Journal of Composite Materials.

PART I. EFFECTS OF WINDING ANGLES ON RESIDUAL STRAINS AND THROUGH-THICKNESS PROPERTIES OF THICK FILAMENT WOUND CYLINDERS

1. INTRODUCTION

Filament winding has matured to become one of major manufacturing process in the fabrication of high performance fiber reinforced composites. As applications of polymer composites increase, there has been a great demand for thick sections of fiber reinforced composites such as flywheel rotors for energy storage system, filament wound hulls for submersibles, and monocoque hulls for armoured fighting vehicles [1~3]. However, such thick sectioned structures inevitably generate residual stresses which mostly deteriorate the structural performance [4,5]. Attempts should be thus made not only to decrease such residual strains but also to predict them in a design process [6].

Most design for filament wound structures was based on netting analysis which uses the in-plane material properties. It was simple and widely accepted particularly for relatively thin sectioned structures. However, as the thickness increase, a more sophisticated analysis such as finite element methods is needed, and through-thickness material properties should be defined. Recently, attempts were made to determine the through-thickness material properties of FRP materials [7,8]. In this work, compressive and tensile tests were performed on various perform types such as unidirectional prepreg, continuous hoop wound filaments, 0/90 woven prepreg. However, helically wound structures were not tested for various winding angles. Coefficients of thermal expansion (CTE) of the helical wound structure in the through-thickness direction were never measured: this material property is also very important particularly for analysis of residual strains within the thick wound structures.

Prediction of the residual stresses generated during the curing process in thick composite cylinders generally requires an understanding of very complicated multi-physics including a detailed universal rheological model, the process of gelation, cure kinetics, the exotherm and interaction between the cylinder and the mandrel. Several investigators have developed theoretical models of the filament winding and curing

processes [4,5,9~12]. In attempts to reduce the residual strains during filament winding process, a multi-stage cure, or an in-situ cure and a continuous curing process can realize the residual stress advantages over the conventional one-stage cure [13,14]. Nevertheless, the one-stage cure has been still widely used in the composite material industry, and it can be more productive as long as the residual stresses are properly managed. The residual strains are mostly caused by the temperature drop during the cool down process and the chemical shrinkage experienced within the matrix. An effective temperature drop which amounts to the residual strains was determined by measuring the residual strains and using two-dimensional stress analysis [6].

In this study, the effects of the helical winding angles on the through-thickness material properties and the residual strains of the helically wound structures are studied. Two-dimensional stress analysis with an effective temperature drop will be used to estimate the stresses and strains accumulated inside the helically wound structures. The through-thickness material properties such as radial stiffness and strength, and the coefficients of thermal expansion (CTE) for different helical winding angles will be measured and used in the analysis [15]. A destructive split-ring test is then performed to measure the residual strains within the helically wound structures. The measured residual strains will be compared with results from the two-dimensional analysis and three dimensional finite element methods.

2. STRESS AND STRENGTH ANALYSIS

The adjacent layups having the alternating angles [$\pm\phi$] act as orthotropic units, and the helically wound cylinder is assumed to be cylindrically orthotropic. A constant orientation angle ϕ throughout the cylinder is considered, and the stress-strain-temperature relations for an axisymmetric multi-layered cylinder in cylindrical coordinate are given as Figure 1.

$$\begin{pmatrix} \varepsilon_\theta \\ \varepsilon_r \end{pmatrix} = \begin{bmatrix} S_{\theta\theta} & S_{\theta r} \\ S_{r\theta} & S_{rr} \end{bmatrix} \begin{pmatrix} \sigma_\theta \\ \sigma_r \end{pmatrix} + \begin{pmatrix} \alpha_\theta \\ \alpha_r \end{pmatrix} \Delta T_e \tag{1}$$

where σ_r, σ_θ, ε_r, ε_θ are the radial and circumferential stresses and strains, respectively.
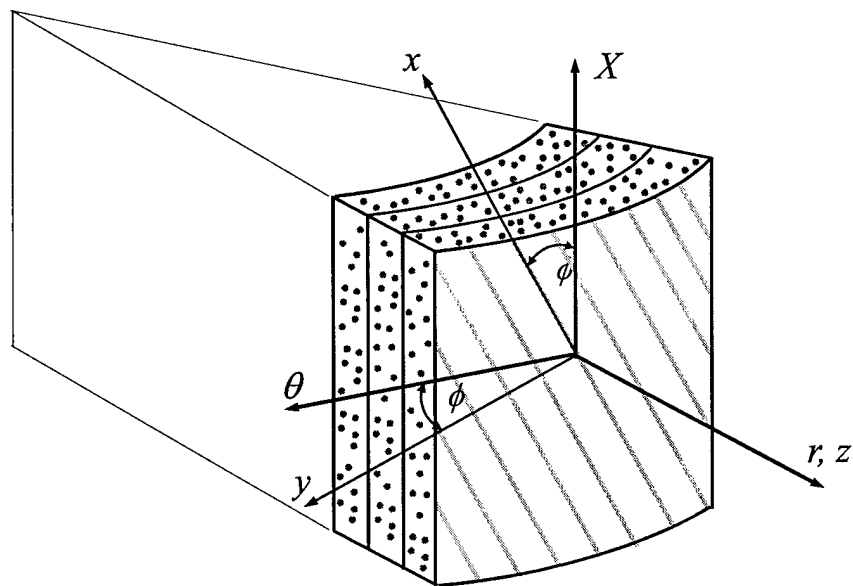
5

Figure 1. Coordinate systems for a helically wound cylinder.

The components of the compliance matrix S_{ij} are obtained by transforming material properties from the material axis to the cylindrical coordinates [16,17]. The axial stresses are assumed to be zero based upon the plane stress assumption. The coefficients of thermal expansion (CTE) α_r and α_θ are also obtained from material properties defined in the material axis. An effective temperature change ΔT_e will be determined to account for the residual strains generated in the cured rotors. The residual strains are mostly caused by the cool down process and the matrix chemical shrinkage.

The equilibrium and compatibility equation together with the stress-strain relationship in Eq.(1) yield the radial and circumferential strains and stresses for a cylinder [16~18]:

$$\varepsilon_r = \kappa C_1 \varphi_1 \bar{r}^{\kappa-1} + \kappa C_2 \varphi_2 \bar{r}^{-\kappa-1} + \varphi_{T2}\Delta T_e \tag{2a}$$

$$\varepsilon_\theta = C_1 \varphi_1 \bar{r}^{\kappa-1} - C_2 \varphi_2 \bar{r}^{-\kappa-1} + \varphi_{T2}\Delta T_e \tag{2b}$$

$$\sigma_\theta = \kappa C_1 \bar{r}^{\kappa-1} - \kappa C_2 \bar{r}^{-\kappa-1} + \varphi_{T1}\Delta T_e \tag{2c}$$

$$\sigma_r = C_1 \bar{r}^{\kappa-1} + C_2 \bar{r}^{-\kappa-1} + \varphi_{T1}\Delta T_e \tag{2d}$$

where the radial coordinate was normalized by the inner radius r_i, and denoted by $\bar{r}$. The symbols κ and φ_i are defined in terms of the material properties:

$$\kappa = \sqrt{\frac{S_{rr}}{S_{\theta\theta}}} , \quad \varphi_1 = \kappa S_{\theta\theta} + S_{\theta r} , \quad \varphi_2 = \kappa S_{\theta\theta} - S_{\theta r} , \tag{3a}$$

$$\varphi_{T1} = \frac{\alpha_r - \alpha_\theta}{S_{\theta\theta} - S_{rr}} \quad \text{and} \quad \varphi_{T2} = (S_{rr} + S_{\theta r})\varphi_{T1} + \alpha_r \tag{3b}$$

Unknown constants C_1 and C_2 are determined from the boundary conditions: zero radial stresses at the inner and outer surfaces in Eq. (2d). For a cylinder of multi rings, the radial stress and displacement continuity conditions should be met at each ring interface. It is noted that every radial coordinate in Eq. (2) is expressed in terms of the normalized radius $\bar{r}$. We can thus conclude that the residual stresses are the same for the cylinders with the geometric similarity.

3. EXPERIMENTS

Three different winding angles, i.e., ϕ=90 (hoop winding), 75 and 60 degrees were considered in this study in order to investigate the effects of the winding angles on the residual strains and through-thickness properties of the cylinders. The cylinders are referred to as H90, H75, and H60, respectively. The ratio of the outer radius to the inner radius of all cylinders is given as 3: they have the same inner radius of 37.5 mm and outer radius of 112.5 mm. The cylinder specifications were summarized in Table 1.

Manufacturing Thick Helical Wound Cylinders

E-Glass fibers (RS2300-366, Owens Corning) were wound over the steel mandrel of 37 mm outer radius, following wet impregnation through a resin bath. Resin system was prepared by mixing epoxy, catalysis and accelerator with the mass fraction ratio of 60:35:5. The resin viscosity was maintained the lowest possible so as to minimize any possible air bubbles that cause voids. During the whole filament winding process, the fiber tension was kept as 10 N, and the revolution speed of the mandrel as 50 rpm. The nose which fed the fibers was axially traveled at the speed regulated to generate the desired helical angles. Filament winding process was then followed by curing in the autoclave with the cure cycle as shown in Figure 2. In order to ensure the axisymmetric material properties, the one end of the horizontal mandrel shaft was connected to the motor and revolved with the rotational speed of 15 rpm during the whole curing process.

Measurement of Through-Thickness Mechanical Properties

After cure and subsequent removal from the mandrel, the cylinder was sliced and machined, yielding the length of 25.4 mm. Cylinders were then cut with a water cooled diamond saw into 2.5 mm thick specimens for radial tensile tests as shown in Figure 3. Two strain gages were bonded onto both surfaces and tensile loads were applied using Tinius Olsen T1000 universal tester with 1 mm/min displacement rate.

Specimens for measuring the CTE in the radial and circumferential directions were also prepared from the cylinders as shown in Figure 4. For each specimen, two high temperature strain gages (WK-06-062AP-350, Micro-Measurement) were bonded onto
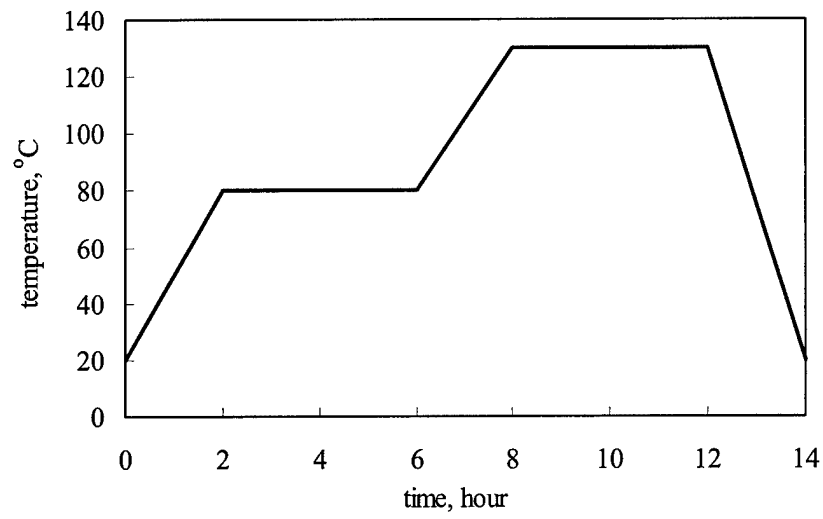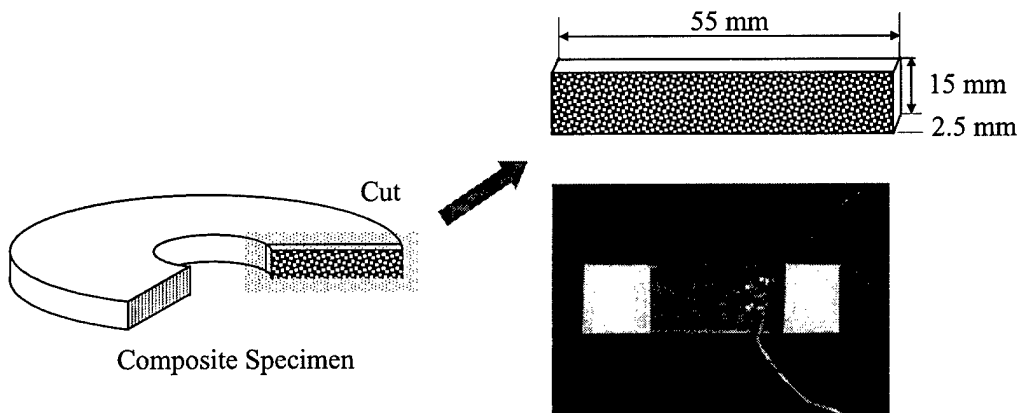
Figure 2. Temperature cure cycles.

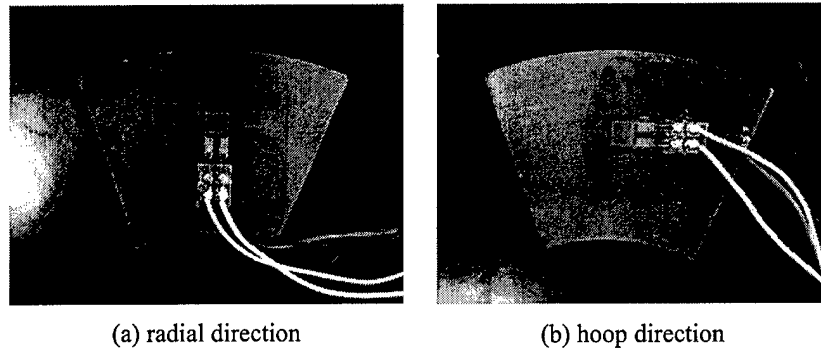**Figure 3**. Specimen configuration for tensile testing.

<table>
<tr><td></td><td>(a) radial direction</td><td>(b) hoop direction</td></tr>
</table>

Figure 4. Pie shaped Specimen to measure the CTEs of Glass/Epoxy cylinder.

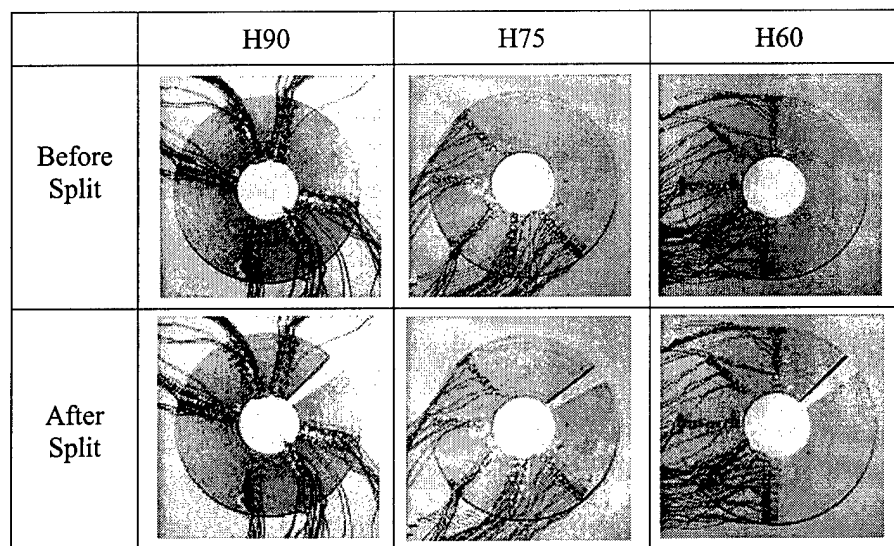|	H90	H75	H60
Before Split			
After Split			

Figure 5. Three specimens H90, H75 and H60 before and after split tests.

both surfaces of the specimen. For a full bridge circuit, the other two strains were bonded to an ultra-low expansion titanium silicate for temperature compensation of dummy gages [15]. An adhesive M-Bond 610 was used for high temperature adhesive. The gage excitation voltage was kept as 2.0 V to avoid self heating due to the current. The specimens and dummy gages were heated from $20\,^{\circ}C$ to $80\,^{\circ}C$. The averaged slope of the measured thermal strains over the temperature range was taken as the CTE.

Measurement of Residual Strains

The main purpose of this research is to determine the residual strains in filament helical wound cylinders according to winding angles. Before measuring the residual strains by the destructive split ring methods, we performed a non-destructive Liquid Penetration (LP) test to examine the cracks or delaminations exposed to the surfaces [19]. From the previous experiments [6], the rings with the lager radius ratios can have the delaminations due to the residual strains generated in the cure process. This LP test can be easily performed to visualize any surface crack, and its standard procedures are well described in ASTM E165 and ISO 3879. Once LP tests are done, side surfaces were polished. Two sets of strain gages, each for radial and hoop direction, were then bonded on both surfaces of the cylinder as shown in Figures 5. Each set consisted of from 5 to 15 stain gages depending on the size of the cylinders. The overall residual strains were first released by splitting the cylinder in the radial direction as shown in Figure 5.

4. RESULTS

Young's Moduli, tensile strengths, and CTE in the through-thickness direction (radial direction) of the helically wound structure for 90, 75, and 60 degree helical angles were measured and listed in Table 3, where the average values of five specimens with the standard deviation were shown. The through-thickness properties are slightly changed as the winding angles decrease: the radial Young's Moduli for 90, 75, and 60 winding angles were measured as 10.41, 10.56, and 10.82 GPa; the coefficients of thermal expansion as 28.08, 29.62, and 30.04 x $10^{-6}/^{\circ}C$; and the tensile strength as 29.14, 25.59, and 24.70 MPa. Such decrease along with the winding angles are thought to be mostly due to the

11

interlaminar shear stresses at the free edges generated by the different contractions along the transverse fiber and matrix directions. Another source may be from the matrix rich zones at the interface between layers of the angle-ply laminates. A further investigation should be performed to understand such variations using detailed analysis such as micromechanics.

One of major objectives in the current research is to measure and predict the residual strains within helically wound structures. The residual radial and hoop strains measured from the cylinders of three different winding angles 90, 75, and 60 degree are shown as square dots in Figure 6. The data show the measured strains after split minus those before split and thus represent the residual strains present in the structures. Whereas the residual strains in the circumferential directions are slightly increasing with the decrease of winding angles, the residual strains in the radial direction are significantly decreasing, i.e., 1.23, 0.99, and 0.54 x 10^{-3} for 90, 75, and 60 winding angles. The maximum radial and hoop strains versus the winding angles are shown in Figure 7. The decrease in the radial strains can be very important particularly in a flywheel rotor since the tensile radial stresses are further developed due to the centrifugal forces. An effective temperature change $\Delta T_e = -140\,°C$ is used in the two-dimensional analysis and three dimensional FEM. The material properties of E-Glass/Epoxy used in the analysis are listed in Table 2. The results are in good agreement with the experimental data. The discrepancies between the two-dimensional analysis and the FEM increase as the winding angle decrease. It is probably because the z-directional effects neglected in the two-dimensional analysis emerge in the three-dimensional FEM. The variation of the maximum radial strains along with the outer radius of the cylinders is obtained for three winding angles and shown in Figure 8. It is observed that the maximum radial strains are significantly affected by the outer radius. As noticed in the analysis, the strains are dependent upon only the radius ratio, which means that the residual strains are the same for the cylinders with the geometric similarity.

12
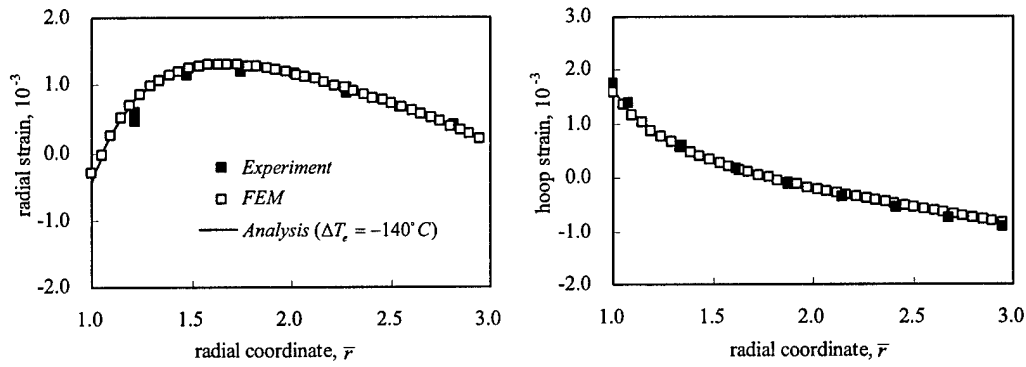
(a) radial and hoop strains of specimen H90
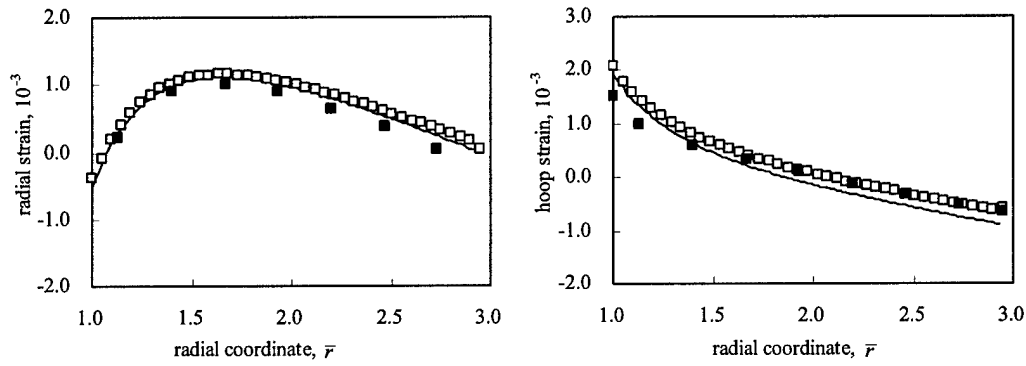
(b) radial and hoop strains of specimen H75
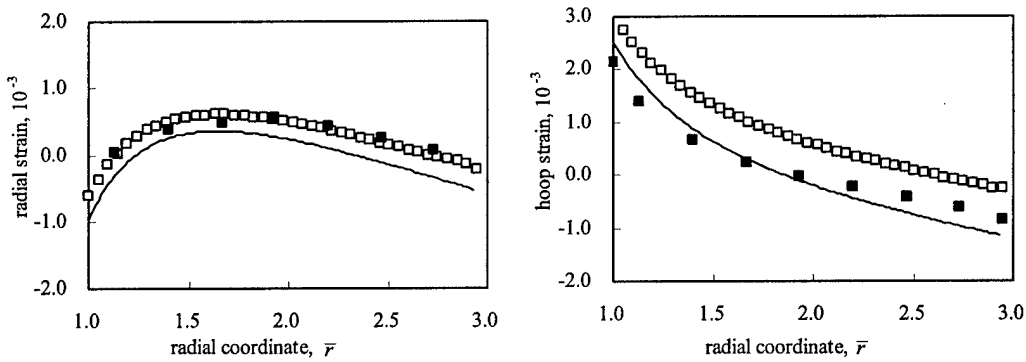
(c) radial and hoop strains of specimen H60

Figure 6. Distribution of radial and hoop strains of helically wound cylinders H90, H75, and H60 along the radius: the experimental data were compared with the two-dimensional analysis and three-dimensional FEM.
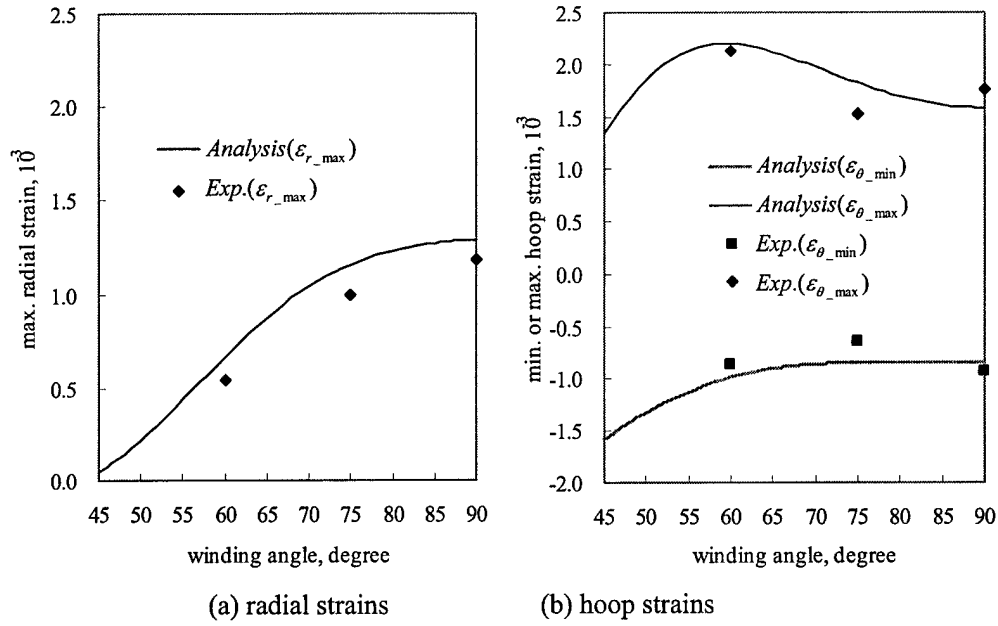
(a) radial strains   (b) hoop strains

Figure 7. Variation of the maximum radial and hoop residual strains with the winding angles.

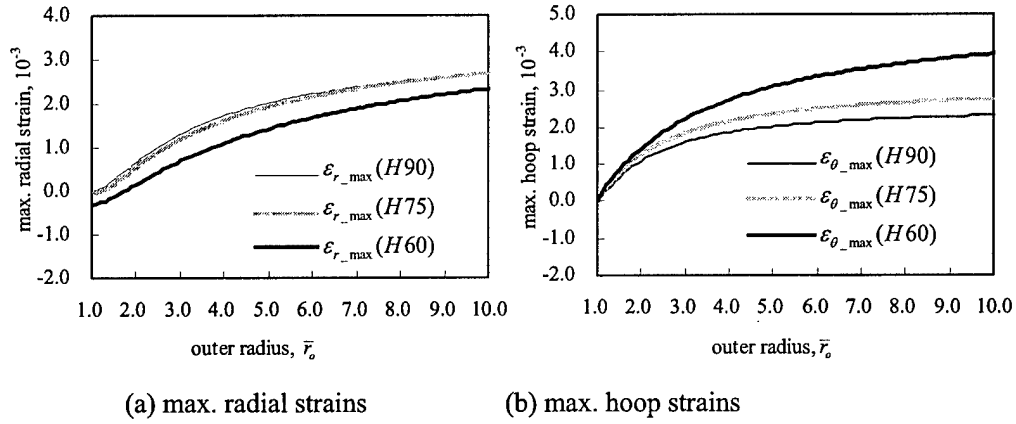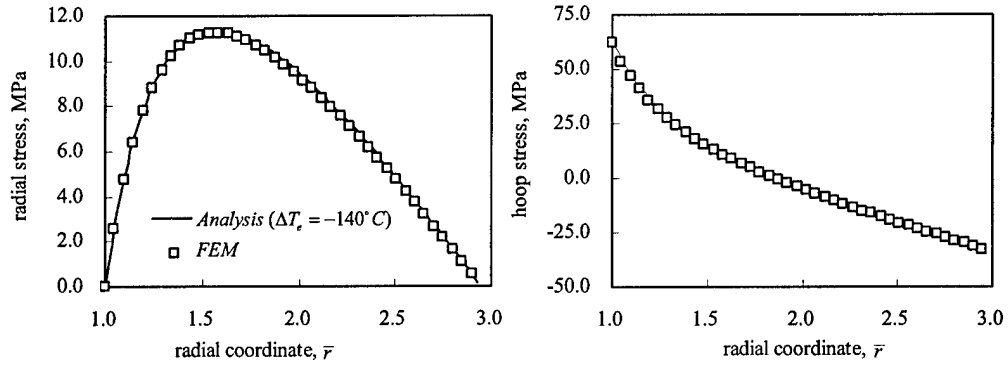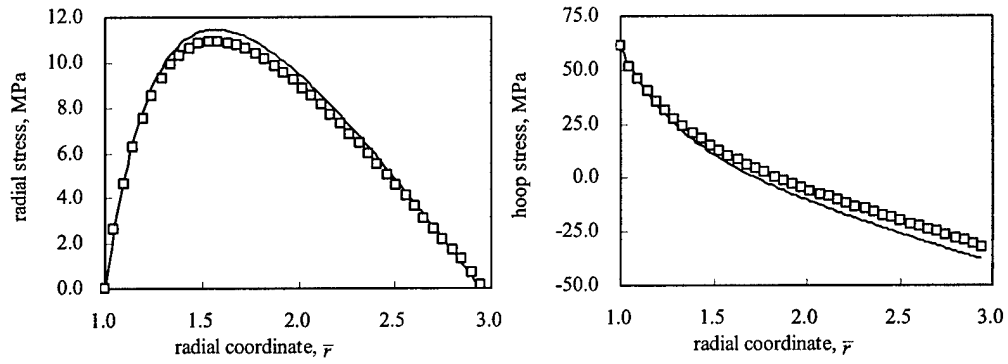(a) max. radial strains   (b) max. hoop strains

Figure 8. Variation of maximum radial and hoop residual strains along the outer radius ratios for three different winding angles 90, 75, and 60 degrees.

(a) radial and hoop stresses of specimen H90

(b) radial and hoop stresses of specimen H75
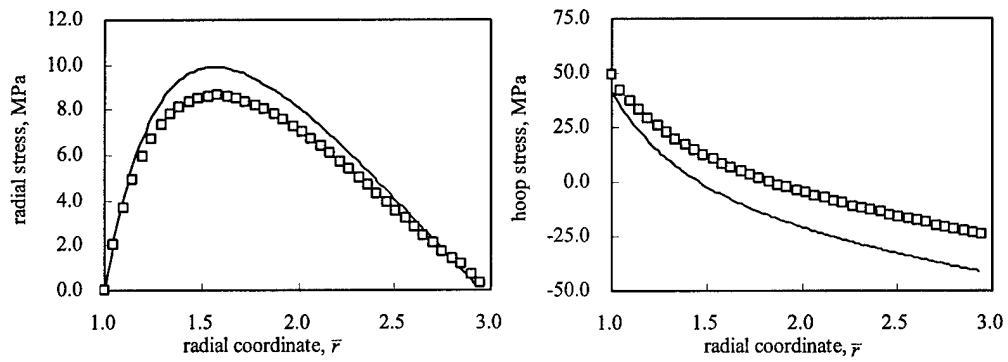
(c) radial and hoop stresses of specimen H60

Figure 9. Distribution of radial and hoop stresses of the helically wound rings along the radius calculated by the present analysis and FEM.

The distribution of the radial and circumferential stresses were also obtained and shown in Figure 9. The maximum circumferential stresses always occur at the inner surfaces whereas the maximum radial stresses occur inside the cylinder. The maximum radial stress of the H90 cylinder reaches as high as 40% of the radial strength. The circumferential stresses, tensile at the inner surface and compressive at the outer surface, generate the bending moment inside the radial surface, which tends to rotate the radial surface once split. Such bending moment is also related to the tensile radial stresses noticed in this study.

5. CONCLUSION

We have measured the through-thickness material properties and the residual strains of helically thick wound cylinders. Whereas the radial stiffness remains almost the same from 90 to 60 degree winding angles, about 7 % increase of CTE and about 17 % decrease of the radial strengths was observed. Such variations of the material properties with the winding angles are believed to be due to interlaminar shear stresses at the free edges generated by the different contractions along the transverse fiber and matrix directions in the test specimens. It is believed that such variations can be better explained using a detailed analysis such as micromechanics approach. The maximum residual strains in the radial direction were observed to decrease by about 54% from H90 to H60 cylinders whereas the maximum residual strains in the hoop increase by about 25%. Such decrease in the radial direction can be effectively utilized in the application for flywheel rotors in which the radial strengths are crucial in supporting the centrifugal forces. Design of such rotors often requires an optimization procedure together with the structural analysis that should consider the residual strains.

Table 1. Specification of the helically wound rings for measurement of residual strains.

Name	Specimen H90	Specimen H75	Specimen H60
Ratio (r_o/r_i)	3.0	3.0	3.0
r_i (mm)	37.5	37.5	37.5
r_o (mm)	110.5	110.5	110.5
Material	E-Glass/Epoxy	E-Glass/Epoxy	E-Glass/Epoxy
Length (mm)	25.4	25.4	25.4
Winding angle	90° (hoop)	75°	60°

Table 2. Material properties of E-Glass/Epoxy used in the analysis

Material Properties	Symbols	Unit	E-Glass/Epoxy
Longitudinal Young's Modulus	E_x	GPa	38.6
Transverse Young's Modulus	$E_y = E_r$	GPa	See **Table 3**.
Stiffness Ratio	κ		2.16
Longitudinal Poisson's Ratio	v_x		0.26
Longitudinal Shear Modulus	G_x	GPa	4.14
Longitudinal CTE	α_x	$10^{-6}/°C$	6.35
Transverse CTE	$\alpha_y = \alpha_r$	$10^{-6}/°C$	See **Table 3**.
Longitudinal Tensile Strength	X	MPa	1062
Longitudinal Comp. Strength	X'	MPa	610
Transverse Tensile Strength	Y	MPa	See **Table 3**.
Transverse Comp. Strength	Y'	MPa	118
Longitudinal Shear Strength	S	MPa	72

Table 3. Through-thickness material properties measured from helically wound E-Glass/Epoxy rings.

Winding Angle	E-Glass/Epoxy		
	E_r, GPa	Y, MPa	α_r, $10^{-6}/°C$
90°(hoop)	10.41±0.67	29.14±1.87	28.08±0.31
75°	10.56±1.13	25.59±3.44	29.62±0.63
60°	10.82±2.82	24.70±4.32	30.04±0.22
Average	10.59	26.47	29.24

REFERENCES

1. Anerdi, G. and Brusaglino, G. 1994. "Technology Potential of Flywheel Storage and Application Impact on Electric Vehicles," *12th International Electric Vehicle Symposium (EVS-12),* 1:37-47.

2. Christopher, D. A. and Beach, R. 1998. "Flywheel Technology Development Program for Aerospace Applications," *IEEE AES System Magazine,* 13(6):9-14.

3. Rodriguez, G. E., Studer, P. A. and Baer, D. A. 1983. "Assessment of Flywheel Energy Storage for Space Craft Power System," *NASA Technical Memorandum 85062,* 1983.

4. Hjellming, L. N. and Walker, J. S. 1989. "Thermal Curing Cycles for Composite Rings with Thick Walls and Thermoset Resins," *Journal of Composite Materials,* 23(10):1048-1064.

5. Bogetti, T.A. and Gillespie, J.A. 1992. "Process-Induced Stress and Deformation in Thick-Section Thermoset Composite Laminates," *Journal of Composite Materials,* 26(5):626-660.

6. Ha, S. K., Kim, H. T. And Sung, T. H. 2003. "Measurement and Prediction of Process-Induced Residual Strains in Thick Wound Composite Rings," *Journal of Composite Materials,* To be published.

7. Ferguson, R. F., Hinton, M. J. and Hiley, M. J. 1998 " Determining the Through-Thickness Properties of FRP Materials," *Composite Science and Technology,* 58: 1411-1420.

8. Kitching, R., Tan, A. L. and Abu-Mansour, T. M. N. 1984 "The Influence of Through Thickness Properties on Glass Reinforced Plastics Laminated Structures." *Composite Structures,* 2: 91-104.

9. Lee, S. Y. and Springer, G. S. 1990. "Filament Winding Rings: I. Process Model," *Journal of composites materials,* 24(12):1270-1298.

10. Calius, E. P., Lee, S. Y. and Springer, G. S. 1990. "Filament Winding Rings: II.

Validation of the Process Model," *Journal of composites materials,* 24(12):1299-1343.

11. Lee S. Y. and Springer G. S. 1990. "Filament Winding Rings: III. Selection of the Process Variables," *Journal of composites materials,* 24(12):1344-1366.

12. Cai, Z., Gutowski, T. and Allen, S. 1992. "Winding and Consolidation Analysis for Cylindrical Composites Structures," *Journal of composites materials,* 26:1374-1399.

13. Kim, C. and White, S. R. 2001. " Continuous Curing and Induced Thermal Stresses of a Thick Filament Wound Composite Cylinder," *Journal of reinforced plastics and composites,* 20 (2):166-180.

14. Garbys, C. W. and Bakis, C. E. 1998. "Simplified Analysis of Residual Stresses in in-situ Cured Hoop-Wound Rings," *Journal of Composite Materials,* 32(13):1325-1343.

15. Kim, R. Y. and Crasto, A. S. 1995. "Dimensional Stability of Composites in Spaces: CTE Variations and Their Prediction," *Proceedings of ICCM-10 Whistler, B.C.,* 4:513-520.

16. Tsai, S. W. 1988. *Composites Design,* Dayton, Ohio: Think Composites.

17. Ha, S. K., Yoon Y. B. and Han, S. C. 2000, "Effects of Material Properties on the Total Stored Energy of a Hybrid Flywheel Rotor," *Archive of Applied Mechanics,* 70:571-584.

18. Lekhnitskii, S. G. 1968. *Anisotropic Plates,* New York: Gordon and Breach Science Publishers Inc.

19. Bray, D.E. 1992. *Nondestructive Testing Techniques,* New York: John Wiley & Sons, Inc.

PART II. Effects of Rotor Sizes and Epoxy System on the Process-Induced Residual Strains within Multi-ring Composite Rotors

1. INTRODUCTION

The fiber reinforced composite materials have been successfully used for the flywheel rotors. It is partly due to the anisotropic properties which results in the reduction of the stresses generated by the rotational centrifugal forces [1-4]. Different fibers such as Glass and Graphite fibers can be further combined into multi-ring rotors to reduce the stresses and increase even more performance of the flywheel rotors [5~7]. On the other hand, however, the anisotropic stiffness and coefficients of thermal expansion differing in the radial and circumferential directions inevitably generate the residual tensile radial strains, which significantly deteriorate the performance of the rotor since the radial tensile stresses are mostly sustained by the relatively weak matrix. The process-induced residual strains can be so high that it leads to delamination within thick filament wound rotors [8]. Those residual strains are generally proportional to the temperature drop and chemical shrinkage experienced during the curing process [9~14]. Thus the temperature profile in a curing cycle is a significant process parameter affecting the strength and integrity of the flywheel rotor. Understanding the effects of the resin systems on the residual strains within thick multi-ring rotors is critical in design of the composite flywheel rotors for larger energy storage capacities.

Prediction of the residual strains generated during the curing process in thick composite rotors generally requires an understanding of very complicated multi-physics such as a detailed universal rheological model including cure shrinkage as well as thermal strains, the process of gelation, cure kinetics, the exotherm and interaction between the rotor and the mandrel. Several investigators have developed theoretical models of the filament winding. Among several attempts, Springer et al. modeled the processes applicable to the moderately thick rings by establishing submodels, each for thermochemical behavior, fiber motion, void, and stress, and developed a cure simulation computer program called WINDTHICK [11~13]. A simplified approach using an

20

effective temperature drop which was verified using the WINTHICK was successfully used to predict the redial strains within rotors of Graphite/Epoxy [8]. However, the effects of cure cycles and Epoxy system on the residual strains have never been pertinently addressed.

Multi-ring type material hybridization in flywheel rotors has been very effectively used to reduce the tensile stresses in the radial direction generated by centrifugal forces [5~7]. Generally, arrangement of softer materials at inner sides and harder materials at outer sides results in the reduction of radial tensile stresses. Several rotors were optimally designed which maximize the overall performance of the flywheel energy storage system. A structural analysis in the design procedure considered both centrifugal forces and the temperature drop that occurred during the curing process [6, 7]. However, the residual stresses within thick multi-ring rotors have never been experimentally measured and quantified so far.

In this study, the effects of the different epoxy systems cured at different temperature profiles and the dimensional size on the residual strains within the hybrid multi-ring rotors will be discussed. Rotors of various sizes will be manufactured using Glass and Graphite fibers with different epoxy systems. The radial stiffness and strength and the coefficients of thermal expansion will be measured to evaluate the characteristics of the epoxy systems. A non-destructive liquid penetration tests [15] will be performed to visually examine the radial delamination, followed by a destructive split-ring test to measure the residual strains [8,16,17]. An effective temperature will be then determined and the residual stresses and strains will be estimated using a stress analysis. The main purpose of this research is to find an epoxy system which will lower residual strains within the hybrid rotors while maintaining the radial strengths as high as the conventional high temperature cured rotors.

2. STRESS AND STRENGTH ANALYSIS

The radial delamination can occur within a ring due to residual stresses. A maximum stress criterion is used for the creation of delamination [19]:

$$\frac{\sigma_r}{Y} = D_\sigma \qquad (1)$$

Delamination occurs when the delamination index D_σ reaches the value of one. Once a delamination occurs, the ring is assumed be split into two rings. The radial location $\bar{r}_{\sigma\_max}$, where the maximum radial stress occurs, can be determined from the stress analysis using Eqs (2~3) in Part I and the boundary conditions for hybrid rotors. The maximum temperature drops ΔT_D which cause an initial delamination can be also obtained using Eqs. (1~4) in Part I. The hybrid multi-ring rotors of the geometric similarity experience a delamination at the same effective temperature drop.

3. EXPERIMENTS

Measurement of Mechanical Properties

Three different matrix systems were considered in this study in order to investigate the effects of the matrix systems on the residual strains within the rotors. Their chemical compound names and mixing ratios were listed in Table 1, each denoted by high, mid, and low temperature epoxy systems (HTES, MTES, LTES, respectively), and the corresponding cure cycles recommended by the resin suppliers were shown in Figure 1. The LTES can be cured alternatively at room temperature for about 48 hours.

Specimens were prepared for measurement of the mechanical properties of the pure resin systems. First, steel mold was machined and specimen with each epoxy system was cured according to the given cure cycles. Strain gages (AE-XX-S30N-350, CAS) were then attached to the specimens, and Young's Moduli and tensile strengths of the pure matrix systems were measured according to the JIS K 6850 specification.

To evaluate the characteristics of the epoxy systems, the radial stiffness and strength and the coefficients of thermal expansion were measured from the Glass and Graphite rotors. The steel mandrel of 37.5 mm outer radius was first machined with two side circular plates of the outer radius of 150 mm and the thickness of 10 mm attached for guiding the winding fiber to produce the rotor of length of 200 mm. Graphite (T300-12K, TORAY) fiber and E-Glass fiber (RS2300-366, Owens Corning) were used, and the fiber tension of 8~10 N was applied during the whole filament winding process. The mandrel

was rotating with the revolution speed of 50 rpm, and the nose which fed the fibers axially traveled at the speed of 1 m/min. The wet filament winding process was then followed by a curing process in the autoclave with the temperature cycles as shown in Figure 1. In order to ensure the axisymmetric material properties, the one end of the horizontal mandrel shaft was connected to the motor and revolved with the rotational speed of 15 rpm during the whole curing process. After cure and subsequent removal from the mandrel, the rotors were sliced and machined using a water cooled diamond saw into 15 mm length rotor. Rotors were then cut with a water cooled diamond saw into 2.5 mm thick specimens for radial tensile tests as shown in Figure 2. The two strain gages were bonded onto both surfaces to measure the radial strains in the tension tests.

Specimens for measuring the CTE in the radial and circumferential directions were also prepared from the rotors as shown in Figure 3. For each specimen, two high temperature strain gages (WK-06-062AP-350, Micro-Measurement) were bonded onto both surfaces of the specimen. For a full bridge circuit, the other two strains were bonded to an ultra-low expansion titanium silicate for temperature compensation of dummy gages [21]. An adhesive M-Bond 610 was used for high temperature adhesive. The gage excitation voltage was kept as 2.0 V to avoid self heating due to the current. The specimens and dummy gages were heated from $20\,^{\circ}C$ to $80\,^{\circ}C$. The averaged slope of the measured thermal strains over the temperature range was taken as the CTE.

Measurement of Residual Strains

The main purpose of this research is to determine the residual strains in filament wound hybrid rotors according to the matrix systems and the rotor sizes. Three two-ring rotors of three different sizes (outer radius ratios $\bar{r}_o$ =1.5, 2.0 and 2.5) for each epoxy system (HTES, MTES, LTES) were prepared using the wet filament winding methods. The same mandrel, side plates, and winding methods were used as for the rotors for measurement of the material properties: all rotors had the inner radii of 37.5 mm. All rotors were hoop wound (90 degree winding angle) using E-Glass fibers for the inner ring and T300-12K graphite fiber for the outer ring with the same thickness. The rotors of different sizes were denoted respectively by R1.5, R2.0, and R2.5, and the specifications were summarized in Table 5. Each series of rotors were then cured in an autoclave

23

according to the epoxy systems, and Rx.x-H, M or L are used to denote a rotor of radius ratio x.x with high, middle or low temperature epoxy systems, respectively. The multi-ring rotors were wet-wound and cured in the same way previously described. The rotors were then removed from the mandrel, and machined into 25.4 mm length rotor.

Before measuring the residual strains, we performed a non-destructive Liquid Penetration (LP) test to examine the delaminations exposed to the surfaces [15]. From the previous experiments [8], it was observed that the rotors with the large radius ratios can have the delaminations due to the residual strains generated in the cure process. This LP test can be easily performed to visualize any surface crack, and its standard procedures are well described in ASTM E165 and ISO 3879. To be brief, the surfaces are first cleaned; a colored liquid is applied to the surface and it may penetrate into the cracks by capillary action; after the removal of any excess, an absorption white layer is applied, drawing the colored liquid out of the cracks and so making them visible. The penetrant, removal and developer were supplied from NAWOO Tech Research Ltd..

Once LP tests are done, the surfaces were cleaned using sand papers, and two sets of strain gages, each for radial and hoop direction, were bonded on both surfaces of the rotor as shown in Figures 4. Each set consisted of from 5 to 15 stain gages depending on the size of the rotors. The overall residual strains within the rotors were released by splitting the ring in the radial direction as shown in Figure 4. A radial slice of about 10 degree containing each row of strain gages was then cut to completely release the residual strains for hybrid rotors. The second cuttings were necessary since the first cut may not completely release the residual strains in the hybrid multi-ring rotors. The readouts before the first cutting were set to zero, and then recorded after first and second cutting.
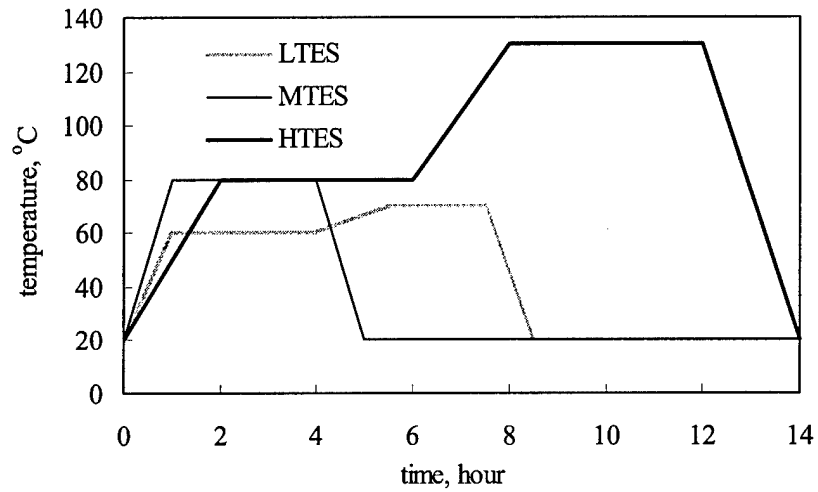
24

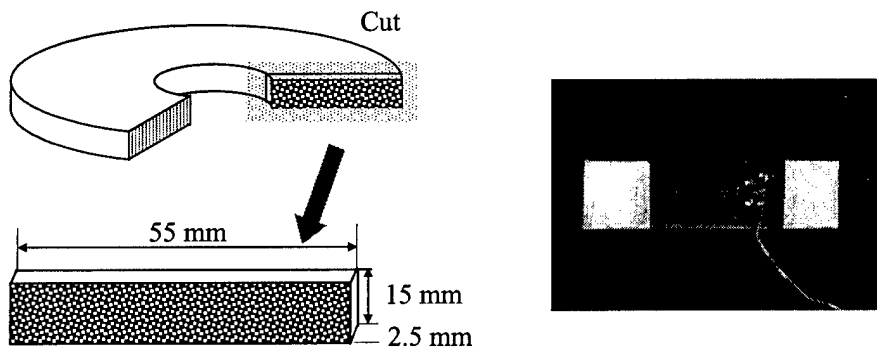**Figure 1**. Three different cure cycles respectively for HTES, MTES, and LTES.
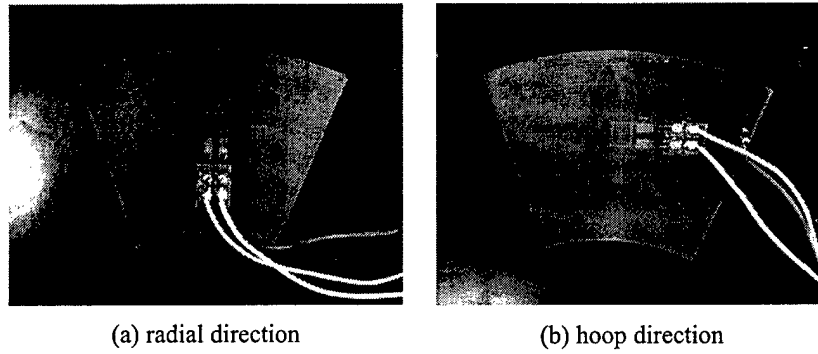

Figure 2. Specimen configurations for tensile tests.

25

(a) radial direction　　　　　　　(b) hoop direction

Figure 3. Pie shaped specimen with the stain gages for measurement of the CTEs.

(a) specimen before split　　(b) specimen after 1st split　　(c) specimen after 2nd split
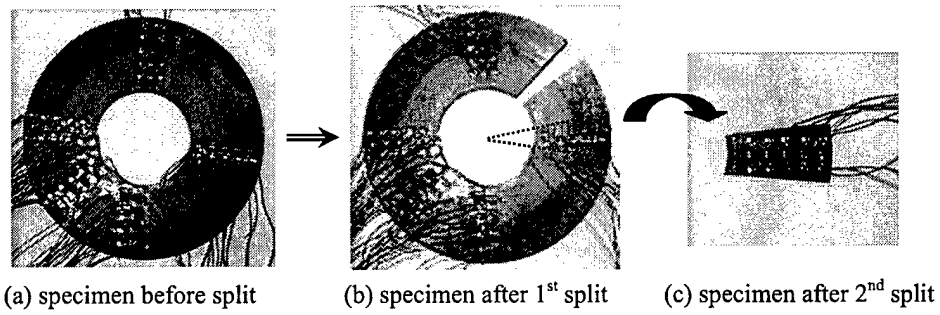
Figure 4. The R2.5-H rotor before and after split in the split-ring test.

4. RESULTS

Material Properties of Three Resin Systems

Young's Moduli and tensile strengths of the specimens of pure matrix systems were measured and their average values with the standard deviation are listed in Table 3. It is noted that the pure MTES has the highest tensile strength (60 MPa) while the pure HTES has the highest Young's Modulus (4.88 GPa). Exact reasons are unknown at this point, but this MTES can be an excellent candidate for the rotor since lower cure temperature can generally lower the residual strains within the rotors.

The resin system can directly affect the radial Young's modulus and tensile strength of the rotors, and their properties were measured from specimen cut from the rotors with three different epoxy systems. Those measured values are listed in Table 3. Among the epoxy systems, the HTES yields the highest stiffness in both rotors of Glass and Graphite fibers: about 5% higher than the rotors with MTES. However, the MTES rotors shows about 2~7% higher strength than the HTES rotors. The LTES in both rotors of Glass and Graphite exhibits about 35% lower strength than other epoxy systems. However, the Young's Moduli shows little variation over the considered epoxy systems.

Besides to the stiffness anisotropy, the difference between the CTE in the radial and circumferential directions is causing the residual strains as noticed in Eqs. (2) and (3) in Part I. The measured CTE of rotors of Glass and Graphite fibers were in Table 4. As expected, the near zero thermal expansion in the circumferential direction was observed in the Graphite rotors. In the case of rotors of Glass fiber, however, the CTE in the circumferential direction is measured as $6.35 \times 10^{-6} / \, ^{\circ}C$, which is about 20% of the CTE in the radial direction. These CTE were measured from the rotors with the MTES, and assumed to be the same for other matrix systems.

Effects of Rotor Sizes on the Residual Strains

One of the main purposes of the current research is to investigate the effects of rotor sizes of the multi-ring rotors on the residual strains. The residual radial and hoop strains measured from the rotors of three different sizes, i.e., R1.5-H, R2.0-H, and R2.5-H (all with HTES) are shown in Figure 5. The data show the strains measured before split

27

minus those before split and thus represent the residual strains present in the cured rotors. Changes in the radial and circumferential strain distributions are due to the material change from E-Glass to Graphite fibers. Differently from the rotor R1.5-H, delaminations are noticed in rotors R2.0-H and R2.5-H from the LP tests as shown in Figure 6. On splitting the specimen, the delaminated surfaces were thus contracted in the radial direction, and discontinuously deformed in the hoop direction, as shown in Figures 5(a) and (b). The effective temperature $\Delta T_e = -140\,^{\circ}C$ was first determined from the rotor R1.5-H, and applied to the other rotors R2.0-H and R2.5-H. The calculated residual strains are shown in Figures 5(a) and (b). The material properties of E-Glass/Epoxy and T300/Epoxy used in the analysis are listed in Table 1 and 2 [19]. The measured properties were used for the epoxy dominant material properties. The calculated strains are in good agreement with the measured residual strains.

The residual stresses of the HTES rotors with $\Delta T_e = -140\,^{\circ}C$ are calculated and shown in Figure 7. The effective temperature drops causing the delamination in each specimen are calculated using Eq. (1): $\Delta T_D = $ -263, -138 and -105 $^{\circ}C$ respectively for specimens R1.5-H, R2.0-H and R2.5-H. Notice that $|\Delta T_e| = 140 > |\Delta T_D|$ for specimens R2.0-H and R2.5-H, indicating occurrence of delaminations ($D_\sigma > 1$). Actually, the effective temperature drop, $\Delta T_e = -140\,^{\circ}C$ yields the damage indices D_σ of 0.53, 1.01 and 1.32 respectively for R1.5-H, R2.0-H and R2.5-H rotors.

Effects of Resin Systems on the Residual Strains

In order to reduce the residual strains, we studied two other epoxy systems which can be cured at lower temperature than the HTES. Rotors were manufactured accordingly, and the residual strains were measured as described in the previous section and shown in Figures 8 for three different rotor sizes. Circles represent the data for the HTES, squares for the MTES, and triangles for the LTES; the data points are average values of least four experimental data.

It is noted in the R1.5 rotors that the residual strains with the MTES were reduced by about 65 % of those with HTES as shown in Figure 8(a). Those reductions in the residual strains were obviously resulted from the lower temperature profile of MTES cure

cycle than HTES. The residual strains of rotors with LTES are as low as those with MTES, but the radial strengths attained only 60% of those with HTES. Effective temperature changes were determined as $\Delta T_e = -50\,^\circ C$ for rotor R1.5-M, and $\Delta T_e = -35\,^\circ C$ for rotor R1.5-L.

The measured residual strains of rotors R2.0 and R2.5 were shown respectively in Figure 8(b) and (c). Whereas we have observed the delaminations in rotors of R2.0-H and R2.5-H, no delaminations were detected in rotors R2.0-M, L and R2.5-M, L. The effective temperatures determined from rotors of R1.5 were used to calculate the residual strains for rotors of bigger sizes and shown in Figures 8(b) and (c). The calculated values are in good agreement with the measured data. It can be concluded that an effective temperature can be used to predict the residual strains of the rotors for different sizes as long as they are made of the same material systems. This observation agreed with the derived results in Section 2, where the residual strains and stresses were expressed in terms of dimensionless radial coordinate.

The residual stresses corresponding to the residual strains were calculated and shown in Figure 9. For rotors of R2.0-H and R2.5-H which experienced delaminations, the stresses without consideration of delaminations were shown to compare the maximum possible stresses. As in the residual strains, significant stress reductions were noticed in rotors with MTES and LTES for all sizes of rotors. The discontinuities in the circumferential stress distribution are obviously due to the material change from Glass to Graphite fibers. It is noted that the maximum radial stresses always occur at the interface between the two rings. This observation can be predicted using the analysis presented in Section 2.

The locations of σ_{r_max} versus the radius ratio $\bar{r}_o$ are calculated and shown as solid lines in Figure 10(a). Since the maximum radial stresses occurs at the ring interface and each ring has the same thickness, the radial locations coincide with the centerline of the overall rotor thickness. The effective temperature changes which cause the delaminations, denoted by ΔT_D (allowable effective temperature drops before delamination), are calculated in terms of the radius ratios $\bar{r}_o$ for each epoxy system and shown in Figure 10(b); $\Delta T_D = -263, -138$ and $-105\,^\circ C$ respectively for rotors R1.5-H, R2.0-H and R2.5-H,

$\Delta T_D = -271$, -143 and $-110\,^{\circ}C$ for rotors R1.5-M, R2.0-M and R2.5-M, and $\Delta T_D = -181$, -96 and $-73\,^{\circ}C$ for rotors R1.5-L, R2.0-L and R2.5-L. The ΔT_D for LTES is quite lower than others since their lower radial strengths. Remember the ΔT_e's for HTES, MTES and LETS were determined respectively as -150, -50 and $-35\,^{\circ}C$. Similarly, the variation of the delaminations indices D_{max} for each epoxy system over the outer radii $\bar{r}_o$ are calculated and shown in Figure 10(c). It is once more observed that the MTES has the lowest delamination indices due to the facts that the MTES rotors have lower temperature drop than the HTES rotors and have the higher radial strength than the LTES rotors. In other words, the higher radial strength together with the lower residual stresses can be achieved in the MTES rotors.

5. CONCLUSION

We have measured and predicted the process induced residual strains within thick hybrid rotors for different matrix systems. As noticed in the results, delaminations can be easily developed within the rotor with the HTES due to the high temperature cure cycles. We have observed delaminations in rotors of the radius ratios greater than 2.0 when using the HTES. The delaminations were clearly observed using both liquid penetration and split ring tests. The residual strains can be reduced significantly using the LTES, but the radial strengths were decreased at the same time. Among the considered epoxy systems, the MTES which needs lower cure temperature than the HTES was found to be the most effective in reducing the residual strains while maintaining as high radial strength as the HTES. The effective temperature drops in calculation of the residual strains was determined as $-50\,^{\circ}C$ for MTES rotors, and no delamination were detected in rotors of radius ratios up to 2.5. The lower residual strains can increase the performance of the rotors: the damage or delamination index 0.34 in the R2.0-M means that the residual strengths, i.e., 0.66 can be used to support the centrifugal forces when used, for instance, as the flywheel rotors.
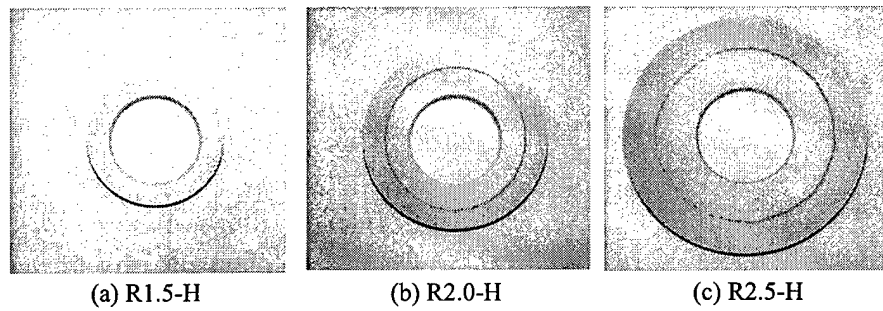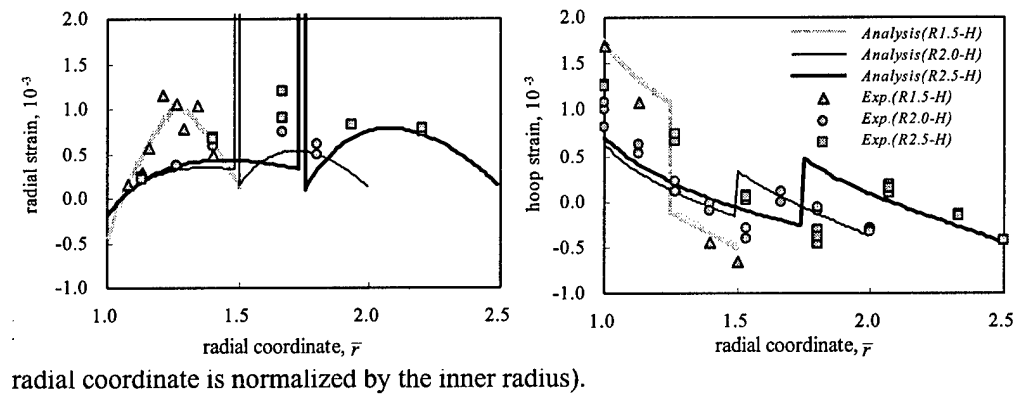
radial coordinate is normalized by the inner radius).

(a) R1.5-H   (b) R2.0-H   (c) R2.5-H

Figure 6. Liquid penetrant test results of R1.5-H, R2.0-H and R2.5-H rotors. The red circles indicate the delamination caused by the residual stresses.
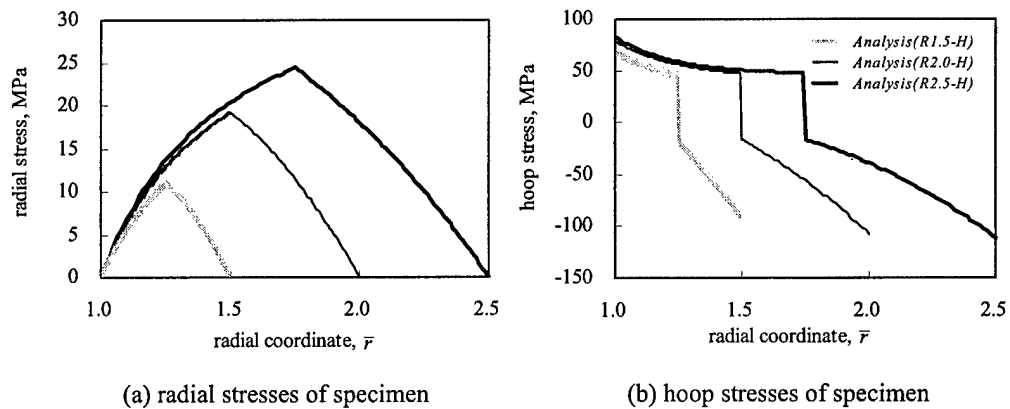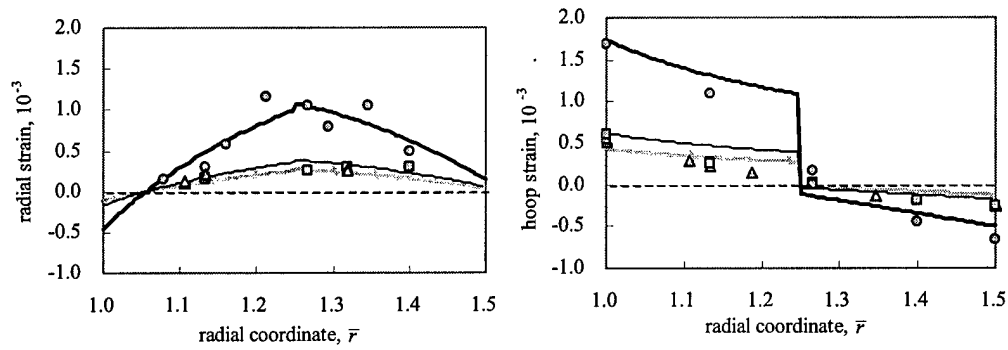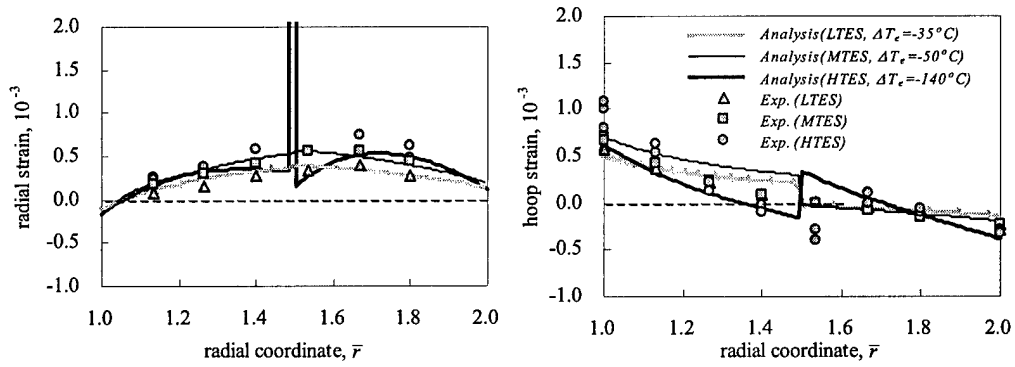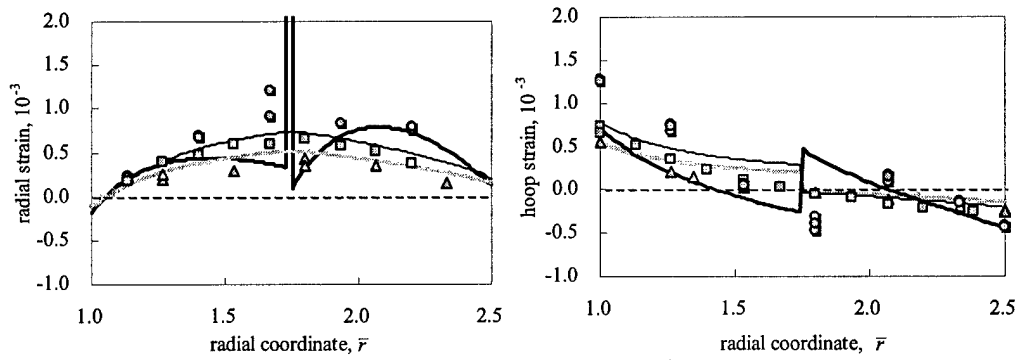

(a) radial stresses of specimen   (b) hoop stresses of specimen

Figure 7. Calculated radial and circumferential stresses of R1.5-H, R2.0-H and R2.5-H rotors without consideration of delamination. (ΔT_e=-140°C)

31

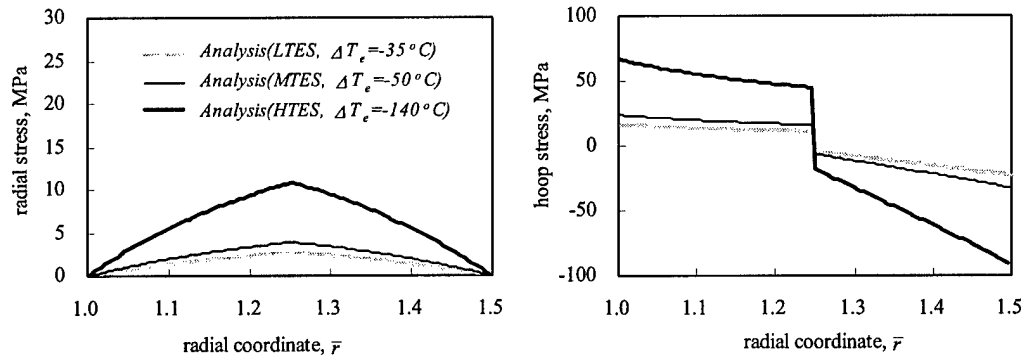(a) radial and hoop strains of specimen R1.5

(b) radial and hoop strains of specimen R2.0

(c) radial and hoop strains of specimen R2.5

Figure 8. Comparison of the residual strains of the R1.5, R2.0, and R2.5 rotors for three different epoxy systems LTES, MTES and HTES.

(a) radial and hoop stresses of specimen R1.5
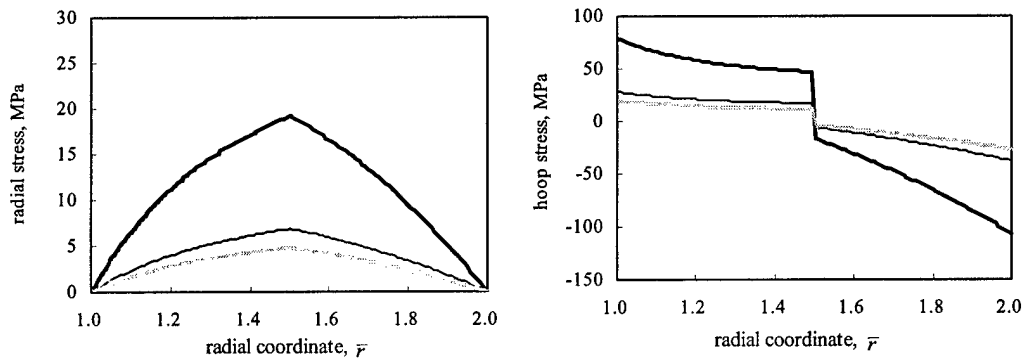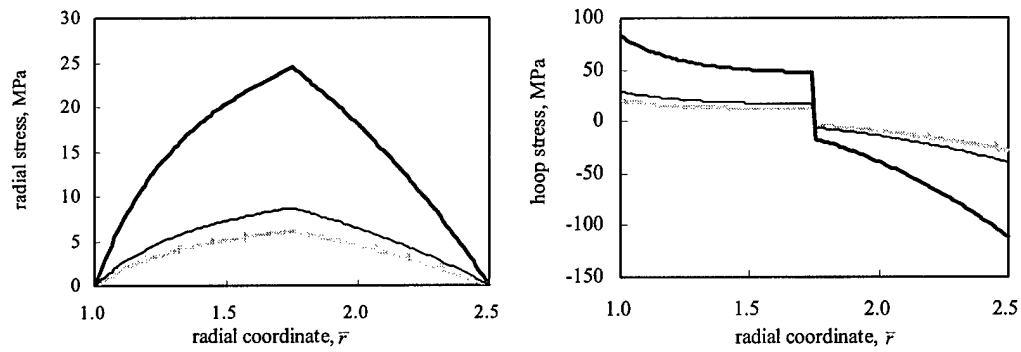
(b) radial and hoop stresses of specimen R2.0

(c) radial and hoop stresses of specimen R2.5

Figure 9. Calculated residual stresses of the R1.5, R2.0, and R2.5 rotors for three different epoxy systems LTES, MTES and HTES.
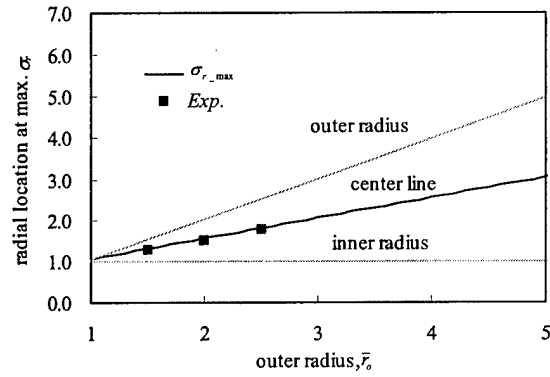
(a) location of maximum radial stresses
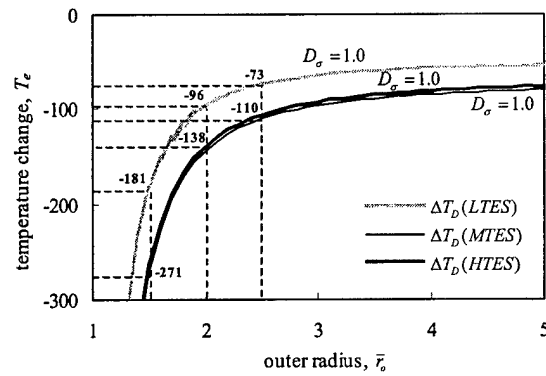
(b) allowable temperature drops before delamination
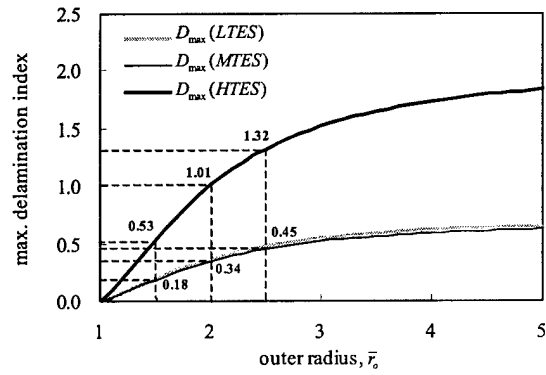
(c) delamination indices

Figure 10. Radial location of maximum radial stresses, allowable effective temperature drop before delamination, and delamination indices versus the radius ratios for three epoxy systems LTES, MTES, and HTES

34

Table 1. Material Properties of three epoxy system considered in this study.

Epoxy system	Resin Type (Commercial Name) Mixture Weight Ratio	Hardener (Commercial Name) Mixture Weight Ratio	Catalyzer (Commercial Name) Mixture Weight Ratio
LTES	Bisphenol-F (SS80-WEH) 80%	Modified Amine (SW1500TKD) 20%	N/A
MTES	Bisphenol-F (SS80-WEH) 75%	Modified Amine (SS-2033H) 25%	N/A
HTES	Bisphenol-F (JF7006) 60%	Acid Anhydride (JF7006H) 35%	Amine (JA001) 5%

Table 2. Material properties of Graphite/Epoxy and E-Glass/Epoxy

Material Properties	Symbols	Unit	Graphite/Epoxy	E-Glass/Epoxy
Longitudinal Young's Modulus	E_θ	GPa	181	38.6
Transverse Young's Modulus	$E_r = E_z$	GPa	See **Table 3**.	
Stiffness Ratio	κ		4.19	2.16
Longitudinal Poisson's Ratio	ν_θ		0.28	0.26
Longitudinal Shear Modulus	G_θ	GPa	7.17	4.14
Longitudinal CTE	α_θ	$10^{-6}/^\circ C$	See **Table 4**.	
Transverse CTE	α_r	$10^{-6}/^\circ C$	See **Table 4**.	
Longitudinal Tensile Strength	X	MPa	1500	1062
Longitudinal Comp. Strength	X'	MPa	1500	610
Transverse Tensile Strength	Y	MPa	See **Table 3**.	
Transverse Comp. Strength	Y'	MPa	246	118
Longitudinal Shear Strength	S	MPa	68.0	72

Table 3. Measured Young's Moduli and the tensile strengths of E-Glass/Epoxy, Graphite/Epoxy and pure epoxy resin specimens.

Epoxy System	E-Glass/Epoxy		Graphite/Epoxy		Pure Epoxy Resin	
	E_r, GPa	Y, MPa	E_r, GPa	Y, MPa	E_r, GPa	Y, MPa
LTES	8.61±0.47	19.12±1.76	8.57±0.18	12.63±1.69	4.15±0.23	49.60±2.61
MTES	8.76±0.60	31.27±3.93	8.44±0.61	18.88±3.54	4.01±0.27	60.03±4.19
HTES	8.89±1.18	29.14±2.74	9.02±0.92	18.41±1.90	4.88±0.27	56.78±4.52

Table 4. Measured CTEs of E-Glass/Epoxy and Graphite/Epoxy specimens.

E-Glass/Epoxy CTE		Graphite/Epoxy CTE	
α_θ	α_r	α_θ	α_r
$6.35\times10^{-6}/\text{°C}$	$28.08\times10^{-6}/\text{°C}$	$0.005\times10^{-6}/\text{°C}$	$25.46\times10^{-6}/\text{°C}$

Table 5. Specifications of the hybrid multi-ring composite rotors for measurement of residual strains.

Name	R1.5	R2.0	R2.5
Ratio (r_o/r_i)	1.5	2.0	2.5
r_i (mm)	37.5	37.5	37.5
r_o (mm)	56.25	75	93.75
Material	E-Glass/Epoxy + Graphite/Epoxy	E-Glass/Epoxy + Graphite/Epoxy	E-Glass/Epoxy + Graphite/Epoxy
Length (mm)	25.4	25.4	25.4
Winding Angle	90°(Hoop)	90°(Hoop)	90°(Hoop)

(Thickness ratio of E-Glass/Epoxy to Graphite/Epoxy rings =1:1)

REFERENCES

1. Anerdi, G. and Brusaglino, G. 1994. "Technology Potential of Flywheel Storage and Application Impact on Electric Vehicles," *12th International Electric Vehicle Symposium (EVS-12)*, 1:37-47.

2. Christopher, D. A. and Beach, R. 1998. "Flywheel Technology Development Program for Aerospace Applications," *IEEE AES System Magazine*, 13(6):9-14.

3. Genta, G. 1985. *Kinetic Energy Storage*, London: Butterworths & Co., Ltd.

4. Grudkowski, T. W., Meyer, T. G. and Wawrzonek, P. H. 1996. "Flywheels for Energy Storage," *SAMPE Journal*, 32(1):65-69.

5. Ha, S. K., Jeong, H. M. and Cho, Y. S. 1998. "Optimum Design of Thick-walled Composite Rings for an Energy Storage System," *Journal of Composite Materials*, 32(9):851-873.

6. Ha, S. K., Yang, H. I. And Kim, D. J. 1999. "Optimal Design of a Hybrid Composite Flywheel with a Permanent Magnet Rotor," *Journal of Composite Materials*, 33(16):1544-1575.

7. Ha, S. K., Kim, D. J. and Sung, T. H. 2001. "Optimum Design of Multi-ring Composite Flywheel Rotor Using a Modified Generalized Plane Strain Assumption," *International Journal of Mechanical Sciences*, 43: 993-1007.

8. Ha, S. K., Kim, H. T. And Sung, T. H. 2003. "Measurement and Prediction of Process-Induced Residual Strains in Thick Wound Composite Rings," *Journal of Composite Materials*, To be published.

9. Hjellming, L. N. and Walker, J. S. 1989. "Thermal Curing Cycles for Composite Rings with Thick Walls and Thermoset Resins," *Journal of Composite Materials*, 23(10):1048-1064.

10. Bogetti, T.A. and Gillespie, J.A. 1992. "Process-Induced Stress and Deformation in Thick-Section Thermoset Composite Laminates," *Journal of Composite Materials*, 26(5):626-660.

11. Lee, S. Y. and Springer, G. S. 1990. "Filament Winding Rings: I. Process Model," *Journal of composites materials,* 24(12):1270-1298.

12. Calius, E. P., Lee, S. Y. and Springer, G. S. 1990. "Filament Winding Rings: II. Validation of the Process Model," *Journal of composites materials,* 24(12):1299-1343.

13. Lee S. Y. and Springer G. S. 1990. "Filament Winding Rings: III. Selection of the Process Variables," *Journal of composites materials,* 24(12):1344-1366.

14. Cai, Z., Gutowski, T. and Allen, S. 1992. "Winding and Consolidation Analysis for Cylindrical Composites Structures," *Journal of composites materials,* 26:1374-1399.

15. Bray, D.E. 1992. *Nondestructive Testing Techniques,* New York: John Wiley & Sons, Inc.

16. Ganley, J. M., Maji, A. K. and Huybrechts, S. 2000. "Explaining Spring-In in Filament Wound Carbon Fiber/Epoxy Composites," *Journal of Composite Materials,* 34(14):1216-1239.

17. Serif, M. A. and Kishaway, H. A. 1999. "Determining Residual Stresses in Thin-Walled Ceramic/Ceramic Composite Pipes," *Journal of American Ceramic Society,* 82(4):977-980.

18. Lekhnitskii, S. G. 1968. *Anisotropic Plates,* New York: Gordon and Breach Science Publishers Inc.

19. Tsai, S. W. 1988. *Composites Design,* Dayton, Ohio: Think Composites.

20. Ha, S. K., Yoon Y. B. and Han, S. C. 2000, "Effects of Material Properties on the Total Stored Energy of a Hybrid Flywheel Rotor," *Archive of Applied Mechanics,* 70:571-584.

21. Kim, R. Y. and Crasto, A. S. 1995. "Dimensional Stability of Composites in Spaces: CTE Variations and Their Prediction," *Proceedings of ICCM-10 Whistler, B.C.,* 4:513-520.

PART III. OPTIMIZATION PROGRAM FOR FLYWHEEL COMPOSITE ROTORS – FLYOPT

1. 2-DIMENSIONAL STRESS & STRENGTH ANALYSIS

For a numerical calculation, the composite flywheel rotor of varying material properties is divided into many rings and each ring is assumed to have a constant material property of an angle-ply laminate $[(\pm\phi)_m]$ as shown in Figure 1. Based on the assumption of a generalized plane strain state, all the rings are free to expand or contract in the axial direction but have the same axial strain. The flywheel rotor is also assumed cylindrically orthotropic and subject to axisymmetric centrifugal forces due to rotation. With the axisymmetric conditions, the circumferential displacements are thus neglected. All the displacements and stresses are thus independent of the axial and circumferential directions. The radial equilibrium equation for each ring and the axial force equilibrium equation for the rotor are concurrently solved and expressed in a stiffness matrix with the radial displacements and the uniform axial strain. Once the displacements and the axial strain are obtained, the stresses and strength ratios are calculated for all the rings.

The stress distribution in each ring is governed by the radial equilibrium equation, which is written in cylindrical coordinates as [24]

$$\frac{d\sigma_r}{dr}+\frac{\sigma_r-\sigma_\theta}{r}+\rho r\omega^2 = 0 \tag{1}$$

where σ_r and σ_θ are the radial and circumferential stresses, respectively, ρ denotes a density, and ω the rotational angular velocity. The stress-strain relation in the cylindrical coordinate system as shown in Figure 1 is written as

$$\sigma = Q(\varepsilon - \alpha\Delta T) = Q\varepsilon - \beta\Delta T \tag{2}$$

where σ and ε are the stress and strain vectors, respectively, Q and α denotes a stiffness matrix and thermal expansion coefficient vector in cylindrical coordinates. Eq. (2) can be

rewritten in the cylindrical coordinate system as

$$\begin{pmatrix} \sigma_\theta \\ \sigma_z \\ \sigma_r \\ \sigma_{\theta z} \end{pmatrix} = \begin{bmatrix} Q_{11} & Q_{12} & Q_{13} & Q_{16} \\ Q_{21} & Q_{22} & Q_{23} & Q_{26} \\ Q_{31} & Q_{32} & Q_{33} & Q_{36} \\ Q_{61} & Q_{62} & Q_{63} & Q_{66} \end{bmatrix} \begin{pmatrix} \varepsilon_\theta \\ \varepsilon_z \\ \varepsilon_r \\ \varepsilon_{\theta z} \end{pmatrix} - \begin{pmatrix} \beta_\theta \\ \beta_z \\ \beta_r \\ \beta_{\theta z} \end{pmatrix} \Delta T \tag{3}$$

In Eq. (3), the axial stress is zero in a plane stress (PSS) assumption and the axial strain is zero in a plane strain (PSN) assumption. More generally, the axial strain is assumed to be a constant in the generalized plane strain (GPS) assumption. Together with these assumptions, the circumferential and radial strains are expressed by the r-direction displacement u_r:

$$\varepsilon_\theta = \frac{u_r}{r}, \varepsilon_r = \frac{\partial u_r}{\partial r}, \varepsilon_{\theta z} = 0, \text{ and } \begin{cases} \sigma_z = 0 & \text{PSS} \\ \varepsilon_z = 0 & \text{PSN} \\ \varepsilon_z = \varepsilon_o & \text{GPS} \end{cases} \tag{4}$$

Substituting Eqs. (3) and (4) into Eq. (1) yields the radial displacement u_r:

$$u_r = -\rho\omega^2 \varphi_0 r^3 + C_1 \varphi_1 r^\kappa + C_2 \varphi_2 r^{-\kappa} + \varphi_3 \varepsilon_o r + \varphi_{T1} \Delta T r \tag{5}$$

C_1 and C_2 in Eq. (5) are unknown constants to be determined from the boundary conditions, and κ and φ_i are defined in terms of the material properties:

$$\kappa = \sqrt{\frac{Q_{11}}{Q_{33}}}, \varphi_0 = \frac{1}{(9-\kappa^2)Q_{33}}, \varphi_1 = \frac{1}{Q_{13} + \kappa Q_{33}}$$

$$\varphi_2 = \frac{1}{Q_{13} - \kappa Q_{33}}, \varphi_3 = \frac{Q_{12} - Q_{23}}{Q_{33} - Q_{11}} \text{ and } \varphi_{T1} = \frac{\beta_r - \beta_\theta}{Q_{33} - Q_{11}} \tag{6}$$

Substitution of Eq. (5) into Eqs. (3) and (4) yields

$$\varepsilon_r = -3\rho\omega^2 \varphi_o r^2 + \kappa C_1 \varphi_1 r^{\kappa-1} - \kappa C_2 \varphi_2 r^{-\kappa-1} + \varphi_3 \varepsilon_o + \varphi_{T1} \Delta T \tag{7}$$

$$\sigma_r = -\rho\omega^2 \varphi_4 r^2 + C_1 r^{\kappa-1} + C_2 r^{-\kappa-1} + \varphi_5 \varepsilon_o + \varphi_{T2} \Delta T \tag{8}$$

where

$$\varphi_4 = \frac{3Q_{33} + Q_{13}}{(9-\kappa^2)Q_{33}}, \varphi_5 = (Q_{31} + Q_{33})\varphi_3 + Q_{32} \text{ and } \varphi_{T2} = (Q_{31} + Q_{33})\varphi_{T1} - \beta_r \tag{9}$$

40

In order to derive the stiffness matrix, the radial displacements at the inner and outer surfaces are written in a displacement vector using Eq. (4),

$$u = \rho\omega^2 u_\omega + \varepsilon_o u_\varepsilon + \Delta T u_T + G\Phi C \qquad (10)$$

where

$$u - \begin{pmatrix} u_{r_i} \\ u_{r_o} \end{pmatrix}, \ u_\omega - \ \varphi_0 \begin{pmatrix} r_i^3 \\ r_o^3 \end{pmatrix}, \ u_\varepsilon - \varphi_3 \begin{pmatrix} r_i \\ r_o \end{pmatrix}, \ u_T - \varphi_{T1} \begin{pmatrix} r_i \\ r_o \end{pmatrix}$$

$$G - \begin{bmatrix} r_i^\kappa & r_i^{-\kappa} \\ r_o^\kappa & r_o^{-\kappa} \end{bmatrix}, \ \Phi - \begin{bmatrix} \varphi_1 & 0 \\ 0 & \varphi_2 \end{bmatrix} \text{ and } C - \begin{pmatrix} C_1 \\ C_2 \end{pmatrix} \qquad (11)$$

In Eq. (11), r_i denotes the inner radius of a ring, and r_o the outer radius of a ring. The normal radial stresses at those two radii can be also written in a force vector using Eq. (8),

$$f_b = \rho\omega^2 f_\sigma + \varepsilon_o f_{\bar\varepsilon} + \Delta T f_{\bar T} + I^* G C \qquad (12)$$

where

$$f_b = \begin{pmatrix} -r_i\,\sigma_{r_i} \\ r_o\,\sigma_{r_o} \end{pmatrix}, \ f_\sigma = -\varphi_4 \begin{pmatrix} -r_i^3 \\ r_o^3 \end{pmatrix}, \ f_{\bar\varepsilon} = \varphi_5 \begin{pmatrix} -r_i \\ r_o \end{pmatrix}, \ f_{\bar T} = \varphi_{T2} \begin{pmatrix} -r_i \\ r_o \end{pmatrix} \text{ and } I^* = \begin{bmatrix} -1 & 0 \\ 0 & 1 \end{bmatrix} (13)$$

Eliminating the constants C in Eqs. (10) and (12) derives the relation of stresses and displacements at the inner and outer surface of each ring. The derived equation can be expressed as

$$ku = f_b + \rho\omega^2 f_\omega + \varepsilon_o f_\varepsilon + \Delta T f_T \qquad (14)$$

The ring stiffness matrix k is

$$k = I^* G\Phi^{-1}G^{-1} = \frac{1}{\zeta_2} \begin{bmatrix} \kappa\zeta_1 Q_{33} - \zeta_2 Q_{13} & -2\kappa Q_{33} \\ -2\kappa Q_{33} & \kappa\zeta_1 Q_{33} + \zeta_2 Q_{13} \end{bmatrix} \qquad (15)$$

where

$$\zeta_1 = \zeta^{-\kappa} + \zeta^{\kappa}, \ \zeta_2 = \zeta^{-\kappa} - \zeta^{\kappa} \ \text{and} \ \zeta = \frac{r_i}{r_o} \tag{16}$$

Notice that, in defining the force term f_b of Eq. (14), the stress component was multiplied by its radius, and the ring stiffness matrix k becomes symmetric. In Eq. (14), f_ω, f_ε and f_T are related to the centrifugal force and defined as

$$f_\omega = \begin{pmatrix} f_{\omega_i} \\ f_{\omega_o} \end{pmatrix} = -f_\sigma + ku_\omega$$

$$f_\varepsilon = \begin{pmatrix} f_{\varepsilon_i} \\ f_{\varepsilon_o} \end{pmatrix} = -f_{\tilde{\varepsilon}} + ku_\varepsilon \tag{17}$$

$$f_T = \begin{pmatrix} f_{T_i} \\ f_{T_o} \end{pmatrix} = -f_{\tilde{T}} + ku_T$$

The constant axial strain ε_o in Eq. (14) can be computed from force balance in the axial direction. Since there is no external axial force applied on the top and bottom surfaces, the summation of the axial forces over all the rings should be zero:

$$\sum_{j=1}^{N} 2\pi \int_{r_i^{(j)}}^{r_o^{(j)}} \sigma_z^{(j)} r \, dr = 0 \tag{18}$$

Using the expressions of σ_z in Eq. (3), and u_r and ε_r in Eqs. (5) and (7), Eq. (18) is expressed as

$$\sum_{j=1}^{N} q^{(j)^T} u + \varepsilon_o \sum_{j=1}^{N} \left(\lambda^{(j)} - q^{(j)^T} u_\varepsilon^{(j)} \right)$$
$$= \rho \omega^2 \sum_{j=1}^{N} \left(q^{(j)^T} u_\omega^{(j)} - \mu^{(j)} \right) + \Delta T \sum_{j=1}^{N} \left(q^{(j)^T} u_T^{(j)} - \chi^{(j)} \right) \tag{19}$$

In Eq. (19), j denotes a ring number and q of a j-th ring is defined as follows (the superscript j is omitted for clarity):

$$q = g^T \Phi^{-1} G^{-1} \tag{20}$$

where

$$g = \begin{bmatrix} \alpha \varphi_1 \left(r_o^{\kappa+1} - r_i^{\kappa+1} \right) \\ \beta \varphi_2 \left(r_o^{-\kappa+1} - r_i^{-\kappa+1} \right) \end{bmatrix} \tag{21}$$

In Eq. (19) and Eq. (21), the following symbols are defined:

$$\lambda = \left[\left(Q_{21} + Q_{23} \right) \varphi_3 + Q_{22} \right] \frac{\left(r_o^2 - r_i^2 \right)}{2}, \mu = -\left(Q_{21} + 3Q_{23} \right) \varphi_0 \frac{\left(r_o^4 - r_i^4 \right)}{4},$$

$$\alpha = \left[\frac{Q_{21} - Q_{23}}{\kappa + 1} + Q_{23} \right], \beta = \left[\frac{Q_{21} - Q_{23}}{(-\kappa + 1)} + Q_{23} \right] \tag{22}$$

$$\text{and } \chi = \left[\left(Q_{21} + Q_{23} \right) \varphi_{T1} - \beta_z \right] \frac{\left(r_o^2 - r_i^2 \right)}{2}$$

Eqs. (1)-(19) apply to any arbitrary ring. At each interface between two adjacent rings (e.g., j and $j+1$), the continuous radial traction and continuous radial displacement should be satisfied:

$$\sigma_{r_i}^{(j+1)} = \sigma_{r_o}^{(j)} \quad \text{and} \quad u_{r_i}^{(j+1)} = u_{r_o}^{(j)} \tag{23}$$

Combining all the ring stiffness matrix in Eq. (14) by using the continuity equations yields the global stiffness matrix equation

$$\begin{bmatrix} K_{uu} & K_{u\varepsilon} \\ K_{\varepsilon u} & K_{\varepsilon\varepsilon} \end{bmatrix} \begin{bmatrix} U \\ \varepsilon_o \end{bmatrix} = \begin{bmatrix} F_b \\ 0 \end{bmatrix} + \rho\omega^2 \begin{bmatrix} F_\omega \\ F_\omega' \end{bmatrix} + \Delta T \begin{bmatrix} F_T \\ F_T' \end{bmatrix} \tag{24}$$

where

$$K_{uu} = \sum_{j=1}^{N} k^{(j)}, \quad K_{u\varepsilon} = K_{\varepsilon u} = \sum_{j=1}^{N} q^{(j)^T} \quad \text{and } K_{\varepsilon\varepsilon} = \sum_{j=1}^{N} \left(\lambda^{(j)} - q^{(j)^T} u_\varepsilon^{(j)} \right) \tag{25}$$

The global displacement vector U consists of $N+1$ displacements at all the radii of the rings. The global force vectors F_b, F_ω and F_T in Eq. (24) are as follows;

$$F_b = \sum_{j=1}^{N} f_b^{(j)} = \left(-r_1 \sigma_{r_i}^{(1)} \quad 0 \quad \cdots \quad 0 \quad r_{N+1} \sigma_{r_o}^{(N)} \right)^T$$

43

$$F_\omega = \sum_{j=1}^{N} f_\omega^{(j)} \,, \quad F_\omega' - \sum_{j=1}^{N} \left(q^{(j)^T} u_\omega^{(j)} \quad \mu^{(j)} \right) \tag{26}$$

$$F_T = \sum_{j=1}^{N} f_T^{(j)} \quad \text{and} \quad F_T' - \sum_{j=1}^{N} \left(q^{(j)^T} u_T^{(j)} \quad \chi^{(j)} \right)$$

Notice that the global stiffness matrix is symmetric, and F_b has only the boundary pressures given at the inner and outer surfaces since the internal stresses were canceled out due to the stress continuity condition. F_ω is an internal inertial force vector due to the rotation.

Now we can solve the system of $N+2$ equations and obtain the radial displacements $u^{(j)}$ at each interface and constant axial strain ε_o. The strains in cylindrical coordinates are then calculated using the relationship in Eq. (4).

The on-axis strains $\bar{\varepsilon}$ in the material symmetric axes are obtained by transforming the off-axis strains ε in the cylindrical coordinates[25] as shown in Figure 2:

$$\bar{\varepsilon} = T\varepsilon \tag{27}$$

where T is a transformation matrix defined in terms of a ply angle ϕ;

$$T = \begin{bmatrix} \cos^2\phi & \sin^2\phi & 0 & \cos\phi\sin\phi \\ \sin^2\phi & \cos^2\phi & 0 & -\cos\phi\sin\phi \\ 0 & 0 & 1 & 0 \\ -2\cos\phi\sin\phi & 2\cos\phi\sin\phi & 0 & \cos^2\phi-\sin^2\phi \end{bmatrix} \tag{28}$$

The on-axis stress $\bar{\sigma}$ is then calculated using the stress-strain relationship:

$$\bar{\sigma} = \bar{Q}(\bar{\varepsilon} - \bar{\alpha}\Delta T) \tag{29}$$

The on-axis stiffness matrix $\bar{Q}$ and the coefficients of thermal expansion (CTE) $\bar{\alpha}$ in Eq. (29) are given by the material properties[25]:

$$\bar{Q} = \begin{bmatrix} 1/E_{\bar{\theta}} & -v_{\bar{\theta}\bar{r}}/E_{\bar{r}} & -v_{\bar{\theta}\bar{z}}/E_{\bar{z}} & 0 \\ & 1/E_{\bar{r}} & -v_{\bar{r}\bar{z}}/E_{\bar{z}} & 0 \\ & & 1/E_{\bar{z}} & 0 \\ sym. & & & 1/G_{\bar{\theta}\bar{z}} \end{bmatrix}^{-1} \quad \text{and} \quad \bar{\alpha} = \begin{pmatrix} \alpha_{\bar{\theta}} \\ \alpha_{\bar{r}} \\ \alpha_{\bar{z}} \\ 0 \end{pmatrix} \tag{30}$$

The definitions of Moduli, Poisson's Ratios, and CTE in Eq. (30) are explained in Table 1.

Once the on-axis stresses in the j-th ring are calculated, a failure of the material can be accessed by using a failure criterion. In this study, 3-dimensional Tsai-Wu quadratic failure criterion[19] is used:

$$\bar{\sigma}^T \tilde{F} \bar{\sigma} + \bar{F} \bar{\sigma} R - R^2 = 0 \tag{31}$$

Solving Eq. (31) yields a strength ratio R indicating material failure with a value greater than 1. When the strength ratio $R < 1$, the applied stresses can increase by a factor of its inverse before material failure occurs. The strength parameters $\tilde{F}$ and $\bar{F}$ are defined in terms of the material strengths:

$$\tilde{F} = \begin{bmatrix} \dfrac{1}{XX'} & -\dfrac{1}{2}\sqrt{\dfrac{1}{XX'}\dfrac{1}{YY'}} & -\dfrac{1}{2}\sqrt{\dfrac{1}{XX'}\dfrac{1}{YY'}} & 0 \\ -\dfrac{1}{2}\sqrt{\dfrac{1}{XX'}\dfrac{1}{YY'}} & \dfrac{1}{YY'} & -\dfrac{1}{2YY'} & 0 \\ -\dfrac{1}{2}\sqrt{\dfrac{1}{XX'}\dfrac{1}{YY'}} & -\dfrac{1}{2YY'} & \dfrac{1}{YY'} & 0 \\ 0 & 0 & 0 & \dfrac{1}{S^2} \end{bmatrix} \tag{32}$$

$$\bar{F} = \begin{bmatrix} \dfrac{1}{X} - \dfrac{1}{X'} & \dfrac{1}{Y} - \dfrac{1}{Y'} & \dfrac{1}{Y} - \dfrac{1}{Y'} & 0 \end{bmatrix} \tag{33}$$

where X and X' are the tensile and compressive strengths in the fiber direction, Y and Y' those in the matrix direction, and S the shear strength.
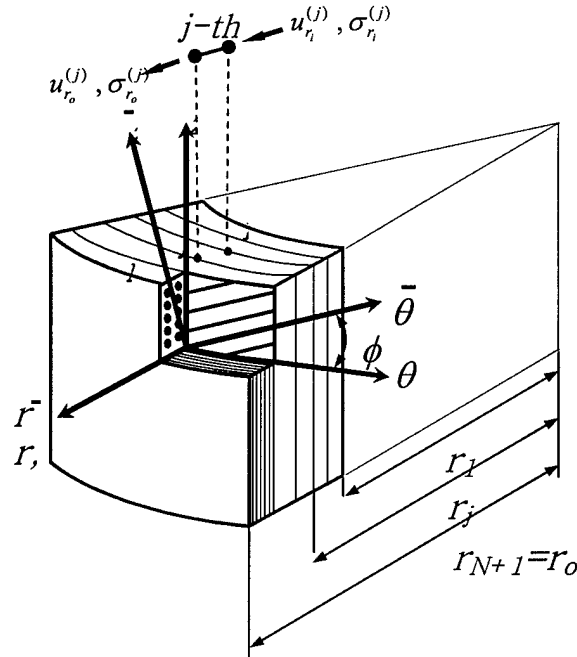
Figure 1. Model of multi-ringed composite flywheel rotor with the angle ply $[(+/-\phi)_m]$ in each rings. The radial displacement and stress of j-th element components, and the off-axis coordinate (θ, z, r) and the on-axis coordinate ($\bar{\theta}$, z, $\bar{r}$) systems are defined.

2. OPTIMIZATION COMPUTER CODE – FLYOPT

A proper combination of composite materials for the rotor could reduce the stress distribution in the rotor and eventually increase TSE. The objective of this study is to maximize TSE of a hybrid flywheel rotor without any material failure. Strength ratio R is used for failure analysis, where a value of R greater than 1 indicates material failure [8]. To ensure the rotor against any material failure, in this approach, strength ratio R and the damage indices D_σ and D_ε calculated at any point of the rotor must have values less than 1. The inner radius r_1 and height h of the rotor are given and the thickness t_m of each rim ($m=1,2,3,...,M$) is used as the design variables. The optimization is then formulated as follows:

$$\textbf{Find} \quad t_m \quad (m=1,2,3,\cdots,M)$$
$$\textbf{Maximize} \quad E = \frac{1}{2}I\omega^2 \qquad (50)$$
$$\textbf{Subject to} \quad \text{Max } R, D_\sigma, D_\varepsilon < 1$$

where I is a mass moment of inertia of the hybrid rotor, and ω is a rotating speed. The total stored energy (TSE) E can be thus written in terms of the inner radius r_m and outer radius r_{m+1} of each m-th rim:

$$E = \frac{\pi}{4}h\omega^2 \sum_{m=1}^{M}\left(r_{m+1}^4 - r_m^4\right)\rho_m \qquad (51)$$

where the subscript m indicates each rim and the other variables include the length of the rotor h, and the density of the m-th rim ρ_m.

In order to solve the nonlinear optimization problem formulated in Eq. (50), the modified method of feasible directions for constrained minimization is used. The main task in the optimization method is to find a usable-feasible search direction and the one-dimensional search. In the every iteration of optimization, stress and strength analysis are performed and the maximum strength ratio in each ring is evaluated as described below.

An optimal design of a hybrid composite rotor, by maximizing TSE without any material failure as formulated in Eq. (50), is performed using a combination of composite materials with different fiber types: (A) Glass/Epoxy, (B) T300/2500, (C) T800H/2500. Optimizations are performed combining up to three different composite rims and can thus be grouped into 3 categories. In the first category, only one material is used, and in the second category, two materials, and so on. In each category only several cases of material selections and sequences are considered because it is efficient way of increasing TSE to arrange softer materials in the inner side and stiffer materials in the outer side of the rotor. The thickness of each composite rim is considered as a design variable and equally divided into element rings, resulting in a total of 30 element rings. The initial thickness for each composite rim is 20 mm, and the inner radius of the rotor is 50mm. The value for the rotating speed is taken as 60,000 RPM.

All the calculated optimum TSE are shown in Figure 2 where each bar indicates the location of each rim and thus the length of the bar means the thickness of each rim. As noted in the stress distribution, the effects of the curing temperature on the optimal design are significant. For instance, the results of the optimal designs using the material sequence A-B-C show that TSE reduces by about 30% with $\Delta T = -110°C$ and 36% with $\Delta T = -125°C$. In other words, neglecting the residual stresses may leads to causing the higher stresses than expected in the process of operating the flywheel rotor. The distributions of the strength ratios for $\Delta T = 0°C$, $\Delta T = -110°C$ and $\Delta T = -125°C$ are shown in Figure 6. It is noted that the maximum TSE is obtained when the strength ratio $R=1$ is reached in every composite rim. Thus, strength is not wasted in each rim which otherwise experience proportionately smaller stress levels. This means that maximizing TSE is equivalent to incorporating the highest possible stresses that satisfy the equilibrium and compatibility conditions. At the optimum state, each thickness of the rim is thus determined so that the strength ratio $R=1$ is reached in every composite rim. It can be obviously noted that the number and sequence of materials are very important in maximizing TSE or minimizing the stresses inside the materials. The stress distributions are effected by the sequence of stiffness, mostly hoop directional Young's modulus. Softer materials inside of the rotor, which are easier to expand in the radial direction, and stiffer materials outside of the rotor, which experience less radial displacement,

48

eventually reduce the radial stresses.

A computer program FLYOPT is developed using Microsoft Excel user-interface. The input data in blue and the output data in red for the user-interface for the optimization are respectively shown in Figures 3. The radial displacement and the stresses are automatically updated according to the results calculated from FlyOpt. The design variables in the optimization module can be linked to any variables in the stress analysis module.
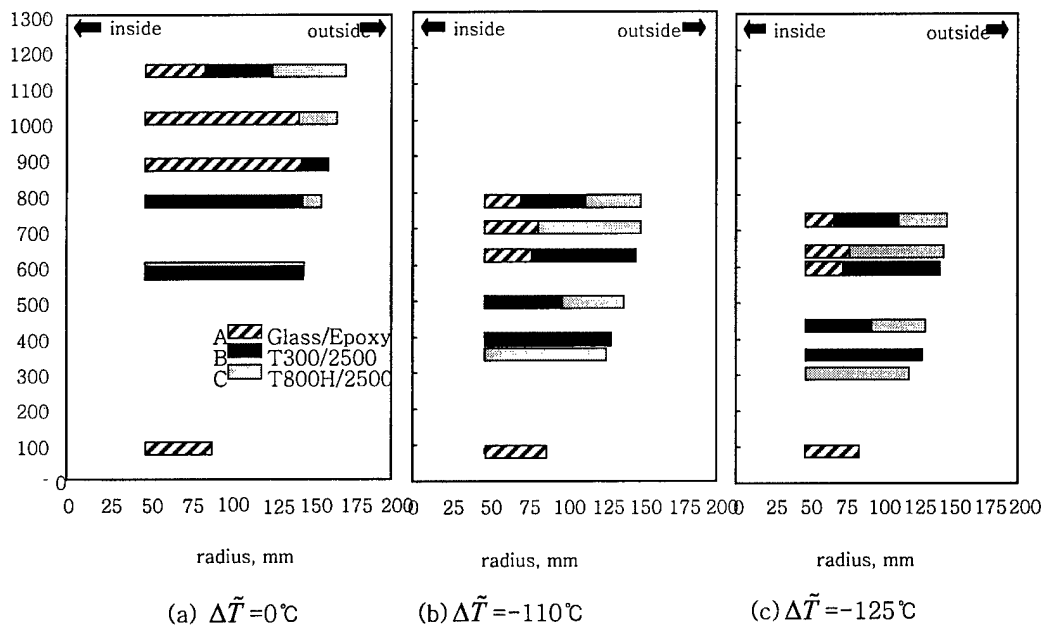

Figure 2. Comparison of optimal thickness of composite rims and the corresponding TSE (Wh) for various selections of composite material (ω=60,000RPM).

QUICK ANALYSIS OF COMPOSITE FLYWHEEL ROTOR

*INPUT:Numbers in Blue
*RESULT:Numbers in Red

Stress Calculation Result Plot

Usable Energy	535.47	Wh
Energy at Burst	769.17	Wh
RPM at Burst	62277	RPM
Max R(GPa)	0.9282	

Burst ω	60000	RPM
Max ω	60000	RPM
Min ω	30000	RPM
r_i	0.05	m
l	0.2	m
P_i	0	Pa
P_o	0	Pa

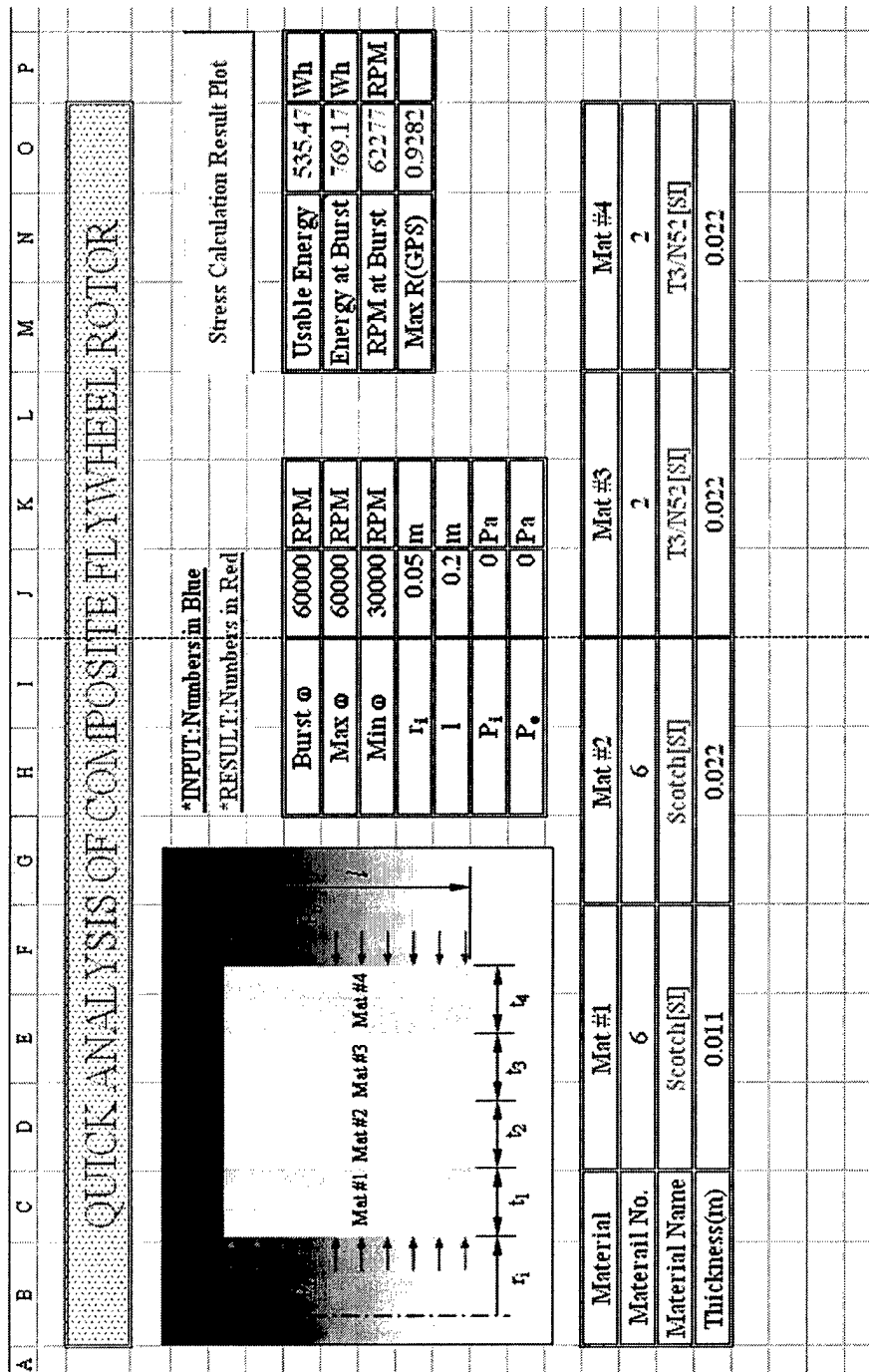| Material	Mat #1	Mat #2	Mat #3	Mat #4
Materail No.	6	6	2	2
Material Name	Scotch[SI]	Scotch[SI]	T3/N52[SI]	T3/N52[SI]
Thickness(m)	0.011	0.022	0.022	0.022

Figure 3. Input data and output results in the optimization module of the program FLYOPT for the flywheel rotor subjected to both the internal pressures and the rotational speed.
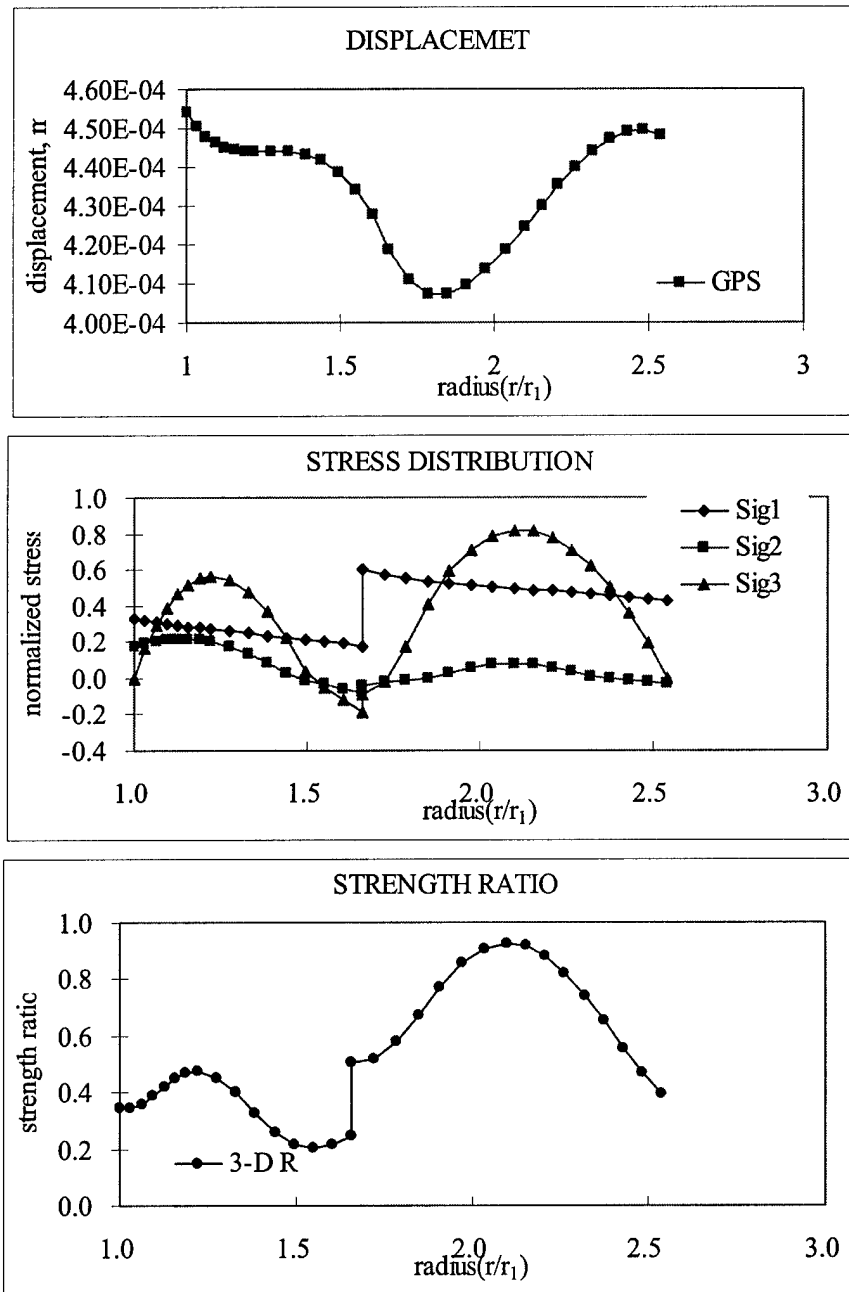
50

Figure 4. The distribution of the radial displacement, the stresses, and the strength ratios; The data are automatically updated according to the results from FLYOPT.

51

3   CONCLUSIONS

The goal of the present work is to develop an optimization tool for a design of the flywheel rotor with a consideration of the process-induced residual strains accumulated during the winding and curing process. A stress analysis of a helically wound hybrid multi-ring rotor is developed in which an equivalent temperature change is used to consider the residual stresses and strains. The validity of the stress analysis has been proved using a three-dimensional finite element program. The effects of the material hybridization and the helical winding angles on the thermal stresses are also investigated. The residual stresses have been experimentally measured using a split-ring test. As a product of this work, a computer program for the optimum design of the hybrid composite flywheel rotor are developed which covers the various size and material properties of the rotor.

REFERENCES

[1]   Anerdi G, Brusaglino G. Technology Potential of Flywheel Storage and Application Impact on Electric Vehicles. *12th International Electric Vehicle Symposium (EVS-12)* 1994;1:37-47.

[2]   Christopher DA, Beach R. Flywheel Technology Development Program for Aerospace Applications. *IEEE AES System Magazine* 1998;13(6):9-14.

[3]   Rodriguez GE, Studer PA, Baer DA. Assessment of Flywheel Energy Storage for Space Craft Power System. *NASA Technical Memorandum 85062*, 1983.

[4]   Genta G. Kinetic Energy Storage. London: Butterworths & Co., Ltd., 1985.

[5]   Grudkowski TW, Meyer TG, Wawrzonek PH. Flywheels for Energy Storage. *SAMPE Journal* 1996;32(1):65-69.

[6]   Post RF, Fowler TK, Post SF. A High Efficiency Electromechanical battery. *Proceedings of the IEEE* 1993;31(3):462-474.

[7]   Danfelt EL, Hewes SA, Chou TW. Optimization of composite flywheel design. *International Journal of Mechanical Sciences* 1977;19:69-78.

[8] Ha SK, Jeong HM, Cho YS. Optimum Design of Thick-walled Composite Rings for an Energy Storage System. *Journal of Composite Materials* 1998;32(9):851-873.

[9] Ha SK, Yang HI, Kim DJ. Optimal Design of a Hybrid Composite Flywheel with a Permanent Magnet Rotor. *Journal of Composite Materials* 1999;33(16):1544-1575.

[10] Ha SK, Kim DJ, Sung TH. Optimum Design of Multi-ring Composite Flywheel Rotor Using a Modified Generalized Plane Strain Assumption. *International Journal of Mechanical Sciences* 2001; 43: 993-1007.

[11] Guemes JA. Curing Residual Stresses and Failure Analysis in Composite Cylinders. *Journal of Reinforced Plastics and Composites* 1994;13(5):408-419.

[12] Hjellming LN, Walker JS. Thermal Curing Cycles for Composite Cylinders with Thick Walls and Thermoset Resins. *Journal of Composite Materials* 1989;23(10):1048-1064.

[13] Bogetti TA, Gillespie JA. Process-Induced Stress and Deformation in Thick-Section Thermoset Composite Laminates. *Journal of Composite Materials,* 1992; 26(5):626-660.

[14] LEE SY, Springer GS. Filament Winding Cylinders: I. Process Model. *Journal of composites materials* 1990;24(12):1270-1298.

[15] Calius EP, LEE SY, Springer GS. Filament Winding Cylinders: II. Validation of the Process Model. *Journal of composites materials* 1990;24(12):1299-1343.

[16] LEE SY, Springer GS. Filament Winding Cylinders: III. Selection of the Process Variables. *Journal of composites materials* 1990;24(12):1344-1366.

[17] Cai Z, Gutowski T, Allen S. Winding and Consolidation Analysis for Cylindrical Composites Structures. *Journal of composites materials* 1992;26:1374-1399.

[18] Herakovich CT, Tarnopol'skii YM. Structures and Design; Handbook of Composites Vol. 2, Amsterdam: Elsevier Science Publishers B.V., 1989, p. 531-582.

[19] White SR, Zhang Z. The Effect of Mandrel Material on the Processing-Induced Residual Stresses in Thick Filament Wound Composite Cylinders. *Journal of Reinforced Plastics and Composites* 1993;12(6):698-711.

[20] Ganley JM, Maji AK, Huybrechts S. Explaining Spring-In in Filament Wound Carbon Fiber/Epoxy Composites. *Journal of Composite Materials* 2000;34(14):1216-1239.

[21] Garbys CW, Bakis CE. Simplified Analysis of Residual Stresses in in-situ Cured Hoop-Wound Rings. *Journal of Composite Materials* 1998;32(13):1325-1343.

[22] Serif MA, Kishaway HA. Determining Residual Stresses in Thin-Walled Ceramic/Ceramic Composite Pipes. *Journal of American Ceramic Society* 1999; 82(4):977-980.

[23] Peri M. An Improved Split-Ring Method for Measuring the Level of Autofrettage in Thick-Walled Cylinders. *Journal of Pressure Vessel Technology, ASME* 1998; 120(2):69-73.

[24] Lekhnitskii SG. Anisotropic Plates. New York: Gordon and Breach Science Publishers Inc., 1968.

[25] Tsai SW. Composites Design. Dayton, Ohio: Think Composites, 1988.

[26] Ha SK, Yoon YB, Han SC. Effects of Material Properties on the Total Stored Energy of a Hybrid Flywheel Rotor. *Archive of Applied Mechanics* 2000;70:571-584.